Master's Thesis

Effizienz und zeitaufgelöste Effizienzmessungen an Pixel-Modulen

Efficiency and timing measurements with pixel-modules

prepared by

Julien-Christopher Beyer

from Braunschweig

at the II. Physikalischen Institut

Zusammenfassung

Das *high luminosity* Upgrade für den Large Hadron Collider (LHC) wird die Luminosität des Beschleunigers auf ein nie zuvor erreichtes Niveau heben. Dabei wird insbesondere der innerste Teil des ATLAS Detektors, der Pixeldetektor, neuen Herausforderungen begegnen. Diese sind zum Beispiel höhere Strahlenschäden sowie bessere Kosteneffizienz. Dafür werden verschiedene Sensorkonzepte für eine neue Pixeldetektorgeneration entwickelt. Um neue Sensorprototypen zu charakterisieren, müssen verschiedene Parameter wie die zeitlich und räumlich differenzierte Effizienz oder der Timewalk bestimmt werden. Zu diesem Zweck wurde ein Lasersystem eingerichtet und getestet sowie verschiedene Analyseverfahren realisiert.

Stichwörter: HL-LHC, ATLAS, Pixeldetektor, Sensorprototypen, Lasersystem

Abstract

The high luminosity (HL) upgrade for the Large Hadron Collider (LHC) will increase the luminosity of the accelerator to a level no other hadron collider has ever reached. Especially the innermost part of the ATLAS detector, the pixel detector, will meet new challenges like increased radiation damage and a need for more cost efficiency. Therefore, different sensor concepts for a new pixel detector generation are under investigation. In order to evaluate new sensor prototypes, different parameters like the time and space dependent efficiency and the timewalk have to be identified. For this purpose, a laser system was set-up and tested as well as several analysis techniques were implemented.

Keywords: HL-LHC, ATLAS, Pixel detector, sensor prototypes, laser system

Contents

Contents

1. Particle Physics

1.1. The Standard Model of particle physics

The Standard Model (SM) represents our current knowledge about particle physics [2]. It is an effective gauge theory whose free parameters are, among others, the masses of the fundamental particles and the strengths of the fundamental forces described by this theory: electromagnetic, weak and strong force.

The particles described in the SM are separated into bosons and fermions. Fermions follow the Fermi-Dirac statistics and have half-integer spin whereas bosons obey the Bose-Einstein statistics and have integer spin. All quarks and leptons are fermions while the force-mediating particles are bosons. The fermions of the SM are further categorized into three generations. The first generation consists of the up-quark (u), the down-quark (d), the electron (e), the electron-neutrino (ν_e) and the corresponding anti-particles. The elementary particle first discovered was the electron. It was found by J.J. Thomson in 1897 using cathode rays [3]. The u and d were proposed in order to explain the growing number of discovered hadrons (bound-states of quarks) in the 1930s and 1940s. Deep-inelastic electron-proton scattering experiments at the Stanford Linear Accelerator Center (SLAC) [4] [5] indicating a substructure of the proton confirmed the early quark model. The second generation of elementary particles consists of the charm-quark (c), the strange-quark (s), the muon (μ), the muon neutrino (ν_μ) and the corresponding anti-particles. The first evidence of a second generation of elementary particles was observed in cosmic-ray studies of C.D Anderson and S. Neddermeyer in 1936. They saw a different curvature of the new particle in a B-field than for any other known particle. Later, it was found to be the μ [6]. The corresponding neutrino, ν_μ, was found using the Alternating Gradient Synchrotron (AGS) neutrino experiment in 1962. They produced a 15 GeV proton beam which was only possible through the invention of strong beam focussing of E.Courant, M.S. Livingston and H. Snyder [7]. The pion beam produced by a fixed target collision with a Be-target was filtered and the remaining neutrinos entered a composition of spark chambers within which some of the neutrinos produced electrons and muons which were very well distinguishable [8].
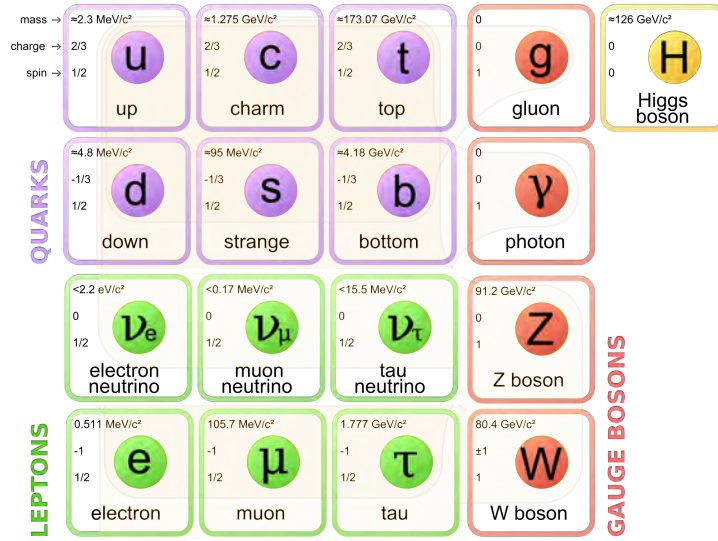
Figure 1.1.: Elementary particles contained in the SM. Leptons and Quarks are grouped in weak isospin doublets.

The second generation of quarks was predicted by S.L. Glashow, J. Iliopoulos and L. Maiani (GIM-mechanism) in 1970 [9], in a time where the strange-quark was known but only little evidence was seen for the charm-quark. The experimental validation was found through the discovery of the J/Ψ meson more or less simultaneously by B. Richter et al. at SLAC [10] and S. Ting et al. at Brookhaven National Laboratory (BNL) [11].

The third generation of elementary particles consists of the top-quark (t), the bottom-quark (b), the tau (τ), the tau neutrino (ν_τ) and the corresponding anti-particles. The explanation of the 1964 found CP violation in the Cronin and Fitch kaon decay experiment [12] was given by M. Kobayashi and T. Maskawa through the introduction of a third generation of quarks [13]. The bottom-quark was found by L.M. Lederman et al. in 1977 at Fermilab [14][15] in Υ-meson decays. Due to the very high mass of the top-quark, its discovery took a little longer since the collider energy was not high enough before. In 1995, the CDF [16] and D0 [17] collaborations at Fermilab claimed the discovery of the top-quark.

The τ was found well before; namely in 1975 by M. Perl et al. at SLAC [18]. He saw a significant number of events of the type $e^+e^- \rightarrow e^-\mu^+ + \geq 4$ particles which is only compatible with the production of an immediately decaying τ pair. The corresponding neutrino, ν_τ, was found after a search initiated by the discovery of the τ. Subsequently, the DONUT (Direct Observation of the NU Tau) experiment at Fermilab found the ν_τ in 2000 and measured some of its properties [19]. Properties of all SM particles are summarized in Figure 1.1.

Besides the quarks and leptons, the gauge bosons play an important role in particle physics as they are the mediators of the different forces. The first known gauge boson was the photon, the mediator of the electromagnetic force. In contrast to the massive gauge bosons ($W^\pm$, Z^0) of the weak force, the photon is massless. The most famous presence of the weak force is the nuclear beta decay where a bound proton turns into a neutron or vice versa. This process was first described 1933 by Fermis contact interaction of four particles (u, d and e^-, ν_e) [20]. Later, a contact-free interaction seemed more likely, including the $W^\pm$ being the mediator of the weak force. First evidence of a Neutral Current (NC) component of the weak interaction was seen 1973 in CERNs Gargamelle bubble chamber where neutrinos penetrated the bubble chamber and various electron traces occurred out of nothing. The only possible explanation was a NC process mediated by the neutral Z^0 boson [21]. The direct measurement of the $W^\pm$ and Z^0 was not made before 1983 at CERNs Super Proton Synchrotron (SPS) which was the first collider with enough energy to produce the quite heavy weak gauge bosons. Necessary for those energies was the newly invented stochastic cooling by S. van de Meer [22]. Subsequently the $W^\pm$ and Z bosons were found by the SPS experiments UA1 [23] and UA2 [24] [25].

The strong interaction is mediated by the gluons. Colour is for the strong interaction what electric-charge is for the electromagnetic interaction. Furthermore, six different colours (three colours and corresponding anti-colours) leads to eight different combinations and thus to eight different gluons. Like the photon, all gluons are massless but in contrast to the photon the gluons also carry the strong charge meaning colour. Thus, gluons do not only couple to quarks (which are the only colourful objects besides gluons themselves) but also with each other making the underlying theory (Quantum Chromo Dynamics QCD) much more complicated than the electromagnetic theory (Quantum Electro Dynamics QED). In 1978, the electron positron collider PETRA at DESY observed three jets events being either quark-anti-quark ($q\bar{q}$) events with gluon bremsstrahlung or three gluon events [26].

The Higgs boson, being the last part of the SM, was predicted by François Englert and Peter Higgs. As the mediator of the Higgs field, and as the result of the electroweak symmetry breaking, it causes the bosons it interacts with to have mass. After a long search at different accelerators, the Higgs boson was discovered in 2012 at CERNs Large Hadron Collider (LHC) simultaneously at both main experiments ATLAS [27] and CMS [28] in the mass region around 126 GeV.

1.2. Experimental basics

In order to investigate particle properties, particle physics experiments are designed to detect and identify the decay products of high-energy collisions. Depending on the type of accelerated particle the accelerator is either built as a ring or as a straight line. The former type is called circular collider because most of the time two beams circulate in opposite direction and the beams are collided at some points. The latter type of accelerator is mainly used with electrons and due to the straight beam-line they are called linear accelerators.

The figure of merit for every accelerator is the center of mass energy which limits the producible mass of particles. Furthermore, the statistics of every experiment is important and thus high luminosities are required. The instantaneous luminosity of an accelerator is defined as

$$\mathcal{L} = f \cdot \frac{n_1 n_2}{4\pi \sigma_x \sigma_y} \tag{1.1}$$

where f is the frequency at which the bunches collide, $n_{1/2}$ is the number of particles in the colliding bunches and $\sigma_{x/y}$ is the spatial size of the bunch in x/y direction [1].

1.2.1. Accelerator physics

The usual way to accelerate a particle is to ionise the particle and put it into an electric field. In a modern particle physics experiment the constant electric field was replaced by so called radiofrequency (RF) cavities. They are built with a specific size and shape so that electromagnetic waves become resonant. Timing of the arrival of particles at the cavity is important because the electrical field inside the cavity oscillates at a given frequency. Entering particles feel a force resulting from the electrical field which transfers energy to accelerate the particles. Once the desired energy of the accelerated particles is reached, they will not be effected by any accelerating voltage any more. However, particles with slightly more or less energy will be accelerated or decelerated through the electrical field.

All circular collider experiments also need to accelerate the circulating particles radially in order to bend the beam on a circular shape. During this radial acceleration, charged particles emit electromagnetic radiation which is named synchrotron radiation. The energy-loss due to synchrotron radiation per circulation [29] is

$$\Delta E = \frac{q^2 \beta^3 \gamma^4}{3\epsilon_0 R} = \frac{q^2}{3\epsilon_0 R} \cdot \frac{E^4}{(m_0 c^2)^4} \tag{1.2}$$

where q is the electric charge of the particle, E its energy, m_0 its mass, R the radius of the accelerator.

Synchrotron radiation is highly dependent on the weight of the particles and thus it is mostly relevant for electrons, even though it becomes relevant also for protons at energies well above LHC energies at comparable radii.

At a circular collider, particle trajectories are bent with a magnetic field in order to hold them on a circular orbit. RF cavities accelerate the circulating particles several times at some points of the ring. In this way, the maximal energy is limited by the magnetic field of the bending magnets and in the case of light particles by synchrotron radiation.

The most important projectile in circular colliders is the proton due to its high mass and the resulting low synchrotron radiation. Nevertheless, the substructure is the most important disadvantage of the proton. It consists of three quarks and more and more sea-quarks become relevant at higher energies. All of these constituents carry a fraction of the momentum of the proton. The center of mass energy of individual reactions is never known exactly because one quark of the proton reacts with one quark of another proton. Consequently, just an unknown fraction of the energy of the proton is available in the reaction.

1.2.2. Particle physics detectors

Various detector concepts are available in order to detect and identify the fragments of high energetic collisions. Typically, different concepts are arranged in a concentric structure around the interaction point in favour of an optimal energy and position resolution. The following part explains different concepts to detect each kind of particle, first given an overview over different particles and afterwards the used detector components are explained.

Charged particles

Relativistic charged particles interact with the matter they are traversing via ionisation and excitation processes of the bound electrons. The energy loss due to ionisation is described by the Bethe-Bloch equation [1],

$$\frac{1}{\rho}\frac{dE}{dx} \approx \frac{-4\pi\left(\hbar c\alpha\right)^2}{m_\mathrm{e}v^2 m_u}\frac{Z}{A}\cdot\left(\ln\left[\frac{2\beta^2\gamma^2 c^2 m_\mathrm{e}}{I_\mathrm{e}}\right] - \beta^2\right), \tag{1.3}$$

where

ρ density of the traversed material

m_u unified atomic mass unit ($m_u = 1.66 \cdot 10^{-27}$ kg)

Z/A ratio of numbers of protons to number of neutrons in the traversed material

β relativistic velocity ($\beta = v/c$)

γ Lorentz factor ($\gamma = \frac{1}{\sqrt{1-\beta^2}}$)

I_{e} the effective ionisation potential (rough approximation: $I_{\mathrm{e}} = (10\,\mathrm{eV}) \cdot Z$).

Though, additional correction terms may be added. The Bethe-Bloch equation mainly depends on $\beta\gamma$ because the Z/A ratio especially is approximately constant for larger values of Z. The energy loss of charged particles is maximal for low values of $\beta\gamma$ and in the high energetic limit it merely increases with a very small slope. Particles with a $\beta\gamma$ value close to the minimum are called minimal ionizing particles (MIPs) which are most frequent in a particle physics experiment. The Bethe-Bloch equation is plotted for different materials in Figure 1.2.
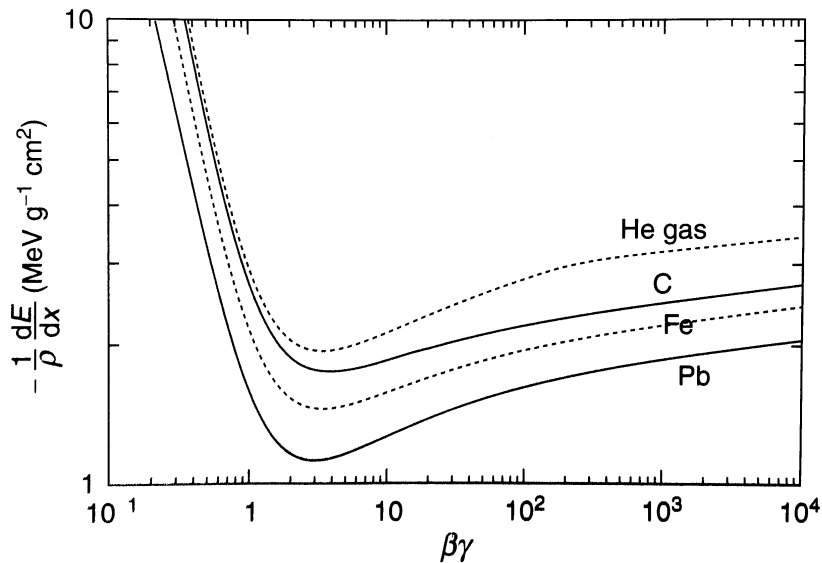
Figure 1.2.: Energy loss of charged particles in different materials predicted by the Bethe-Bloch equation [30].

It is worth mentioning that the derivation of the equation assumes the charged particle to have a mass well above the electron mass and for this reason the Bethe-Bloch equation does not hold for electrons. Nevertheless, there is a modified Bethe-Bloch equation which describes the energy loss of electrons due to ionisation within usable limits. The energy

loss of electrons due to ionisation dominates at low energies. For energies above a critical energy (E_c) the main contribution to the energy loss is due to bremsstrahlung (see next section). The critical energy depends on the charge Z of the nucleus of the penetrated matter and is approximately

$$E_\mathrm{c} \approx \frac{800}{Z}\mathrm{MeV}. \tag{1.4}$$

Bremsstrahlung is not crucial for heavy particles because of the strong dependence of bremsstrahlung to the mass of the particle [31]

$$\frac{dE}{dx} \propto \left(\frac{E}{m}\right)^4. \tag{1.5}$$

Hence, the main contribution to the energy loss of electrons in high energy particle physics experiments, mostly in the multi-GeV range, is due to bremsstrahlung. Furthermore, bremsstrahlung explains what the signal-evolution of an electron in the calorimeter looks like.

Electrons and photons

As mentioned before, electrons lose most of their energy via bremsstrahlung. This process describes the radiation of a photon due to the acceleration of the electron while slowing down in the matter-nuclei's Coulomb-potential. The emitted photon then creates an electron positron pair (pair production) which again causes bremsstrahlung and so on. This cascade is called electromagnetic shower. The electromagnetic shower is short and local. Besides the shower process due to bremsstrahlung, electrons also ionise material while traversing it. This is important especially for tracking detectors, see Chapter 3.

The process to detect photons is very similar compared to that of electrons. Though, here the electromagnetic shower starts with a pair production process. Also the photon is not visible in tracking detectors because there is no ionisation. Besides pair-production there is the photo-effect which describes the transfer of the energy of a photon to a bound electron and the subsequent ionisation. The last mechanism is called compton scattering where an inelastic scattering process of the photon with a charged particle (most of the time an electron) is described.

The energy of both, electrons and photons, are mainly measured within the electromagnetic calorimeter, whereas the momentum of electrons is also measured with tracking detectors.

Quarks, gluons and hadrons

Quarks and gluons produced at the interaction point of a detector immediately hadronize which means they form bound states. This process evolves and leads to a huge amount of indistinguishable particles within a cone. Those structures are called jets. Due to their large amount of mostly charged ($\approx \frac{2}{3}$) particles they form clearly visible signals in all traversed parts of the detector.

Analogously to the electromagnetic showering process, there is also a hadronic shower process. Different types of hadrons are produced through strong interactions between jet-particles and matter-nuclei. All charged particles lose energy as a result of ionisation processes. Due to neutral pion (π^0) production and the associated immediate decay into photons, there is always an electromagnetic component in a hadron shower. The variety of final state particles and the significantly larger typical interaction length of hadronic interactions, compared to the radiation length of electromagnetic interactions, leads to an inherently more variable form of hadronic showers compared to electromagnetic showers.

Taus

Tau leptons are difficult to detect. They decay mostly instantaneously and only the mean decay-length is a few mm, which would be easily measurable with a tracking detector. Instead, the decay products are detected. Those decay products are hadronic but they are also leptonic. In every case neutrinos are produced and an unknown fraction of energy is lost which impedes the reconstruction.

Muons

Muons emit much less bremsstrahlung than electrons because of their significantly larger mass. Hence, ionisation is the only process by which a muon loses energy in the detector. Consequently, muons are not absorbed within the detector but they traverse through it. Therefore, muon identification happens at the outermost part of the detector even if the additional measured points in the inner tracking detector improve the momentum measurement. Muons are also detectable in the tracking detectors and the calorimeters.

Detector components

As mentioned above, the most useful detector design at colliders consists of different layers in an onion-like structure. The following parts are found from the inside to the outside in most of the modern particle physics detectors:

- **tracking detector:** the innermost part of the detector consists of a tracking detector designed to influence the traversing particles as little as possible. The tracking detector is used to reconstruct the trajectories of all particles. It is also possible to measure the momentum of charged particles via a magnetic field as well as the curvature of the trajectory. There the momentum resolution [31] evolves like

$$\frac{\sigma_{p_T}}{p_T} = \frac{\sigma_x p_T}{0.3BL^2} \cdot \sqrt{\frac{720}{N+4}} \qquad (1.6)$$

  where σ_x is the spatial resolution of each detector layer, B is the magnetic field strength, L is the length of the path within the tracking detector, and N is the number of points on this path. As a result, the momentum resolution decreases with increasing momentum.

  Multiple concepts are used as tracking detectors and all of them have their advantages and disadvantages. Due to the focus of this thesis towards semiconductor detectors, there will be a detailed description of semiconductor detectors in Chapter 3. Other tracking detector concepts are gas filled detectors which work as many wire proportional counter. Further it is also possible to detect scintillation light of traversing particles, for example with many scintillating fibres around the interaction point.

- **calorimeter:** the next layer after the tracking detector is usually a calorimeter. The calorimeter is used to measure the energy of individual particles and jets. As the generated heat of jet penetration through the calorimeter is much too small to be observed, a different quantity for measuring is needed. Scintillation light through excitation processes and free charge carriers through ionisation were found to be quantifiable. The former one needs a scintillating material which has to be connected to a photomultiplier in order to measure the generated photons. Free charge carriers are collected with electrodes attached to the penetrated material. These components are called active material due to their characteristic of responding to penetrating particles. Furthermore, the response is proportional to the amount of deposited energy. In order to deduce the entire energy of a jet, it is useful to stop the particle in the calorimeter to record the complete energy deposition.

  There are two common construction concepts. The first is called homogeneous calorimeter and consists uniformly of one active material. The main problem of those calorimeters is the choice of material because it has to fulfil two criteria. It has to be an active material and it should be as dense as possible, which means high-Z material

required to allow compact dimensions while still being able to stop penetrating particles. The second common type are sandwich or sampling calorimeter. They consist of alternating layers of active and passive material. The active material is again used to measure the amount of deposited energy whereas the passive material is used to further develop the shower in order to stop it. Therefore, passive materials are typically very dense in order to minimize the dimensions of the calorimeter.

Electromagnetic and hadronic calorimeters have to be distinguished. The short radiation lengths of electromagnetic showers and thus short longitudinal and lateral extents of electromagnetic showers allow compact dimensions whereas hadronic calorimeters have to be much larger. The energy resolution of an typical electromagnetic calorimeter is in the order [1] of

$$\frac{\sigma_E}{E} \propto \frac{3\,\% - 10\,\%}{\sqrt{E/\text{GeV}}}, \tag{1.7}$$

whereas the energy resolution of a typical hadronic calorimeter is significantly worse. This is mainly caused by fluctuations in the amount of energy lost in nuclear breakup and also the variation of the electromagnetic fraction of the shower. Moreover, the energy contribution of neutrons is invisible due to a low cross-section or rather strongly delayed and therefore not measurable. The energy resolution of a typical hadronic calorimeter [1] is

$$\frac{\sigma_E}{E} \propto \frac{50\,\%}{\sqrt{E/\text{GeV}}}. \tag{1.8}$$

Even if the energy resolution seems not to be very good, it decreases with increasing energy and thus the energy resolution will be better for higher center of mass energies.

- **muon detector:** muons are detected in muon chambers which are located at the outermost part of the detector. Muon chambers are often drift chambers where the traversing charged particles, almost always muons, ionise the gas. Then the ions and electrons drift as a result of an applied electric field to their electrodes and produce a signal. In general, all other particles except neutrinos but which will not interact in the muon chamber either should be absorbed within the calorimeter. For muons the muon chambers provide additional points for the momentum measurement and improve the accuracy.

2. LHC and the ATLAS experiment

2.1. The Large Hadron Collider

Physicists at the LHC are searching for both proofs of the standard model and new physics meaning new particles and new couplings beyond the standard model. High precision measurements are made in order to accurately determine the properties of all particles like their mass, spin and many more. These high precision measurements also provide an opportunity to discover new physics.

For those purposes two things are needed. On the one hand higher center of mass energies are required in order to produce heavier particles. On the other hand high luminosities are demanded to achieve good statistics which in turn are needed to accomplish high precision measurements.

The Large Hadron Collider (LHC) was designed [33] in order to fulfil those requirements. The LHC is built into the tunnel of the Large Electron Positron (LEP) collider at the European Laboratory for Particle Physics (french: Conseil Européen pour la Recherche Nucléaire, CERN).

The tunnel has a length of 26.7 km and is approximately 100 m below ground. The LHC is designed to reach $\sqrt{s} = 14$ TeV and an instantaneous luminosity of $\mathcal{L} = 1 \times 10^{34}\,\mathrm{cm^{-2}\,s^{-1}}$ (further information in Section 2.1.1). The beam is guided through a two-in-one super-conducting magnet structure that surrounds the two separate beampipes. Running at full extent, 2808 proton bunches circulate in each beampipe with a total energy of 664 MJ. The 1232 bending magnets are cooled to a temperature of 1.9 K with a maximal magnetic field of 8.4 T.

A couple of pre-accelerators are needed to provide the desired beam properties for an LHC beam. In addition to the LHC with its experiments, the different pre-accelerators are shown in Figure 2.1; they are mostly old accelerators from previous experiments. The last stage of the beam before the LHC is the Super Proton Synchrotron (SPS) which delivers a 450 GeV proton beam. Eight single-cell superconducting RF cavities accelerate the beam to its final energy within approximately half an hour. The beam has to be dumped about every ten hours by reason of the decreasing beam quality and luminosity
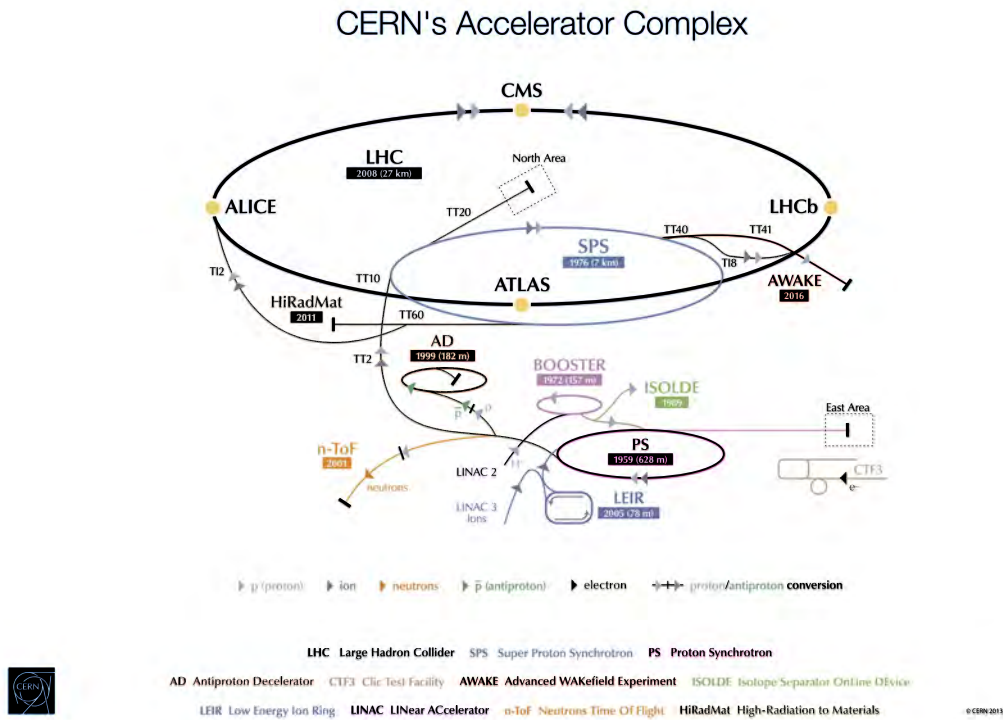
Figure 2.1.: The CERN accelerator complex near Geneva [32].

or whenever unexpected events may cause the beam to damage the facility.

Four experiments are situated in caverns below ground. In those areas the beams are collided and the products of the reaction are measured with different detectors for different purposes. The two multi-purpose detectors of the LHC are the *A Toroidal LHC Apparatus* (ATLAS) and the *Compact Muon Solenoid* (CMS). The other two experiments are the LHCb (b for bottom) and the *A Large Ion Collider Experiment* (ALICE) which are more specialized. As the name indicates, LHCb is specialised on b-physics and ALICE is mainly built to investigate heavy ion collisions (e.g. Pb beams with 5.5 TeV/nucleon). In contrast to the symmetric multi-purpose detectors of ATLAS, CMS and ALICE, LHCb is an asymmetric detector.

2.1.1. Upgrades

The mentioned design-parameters of the LHC were not achieved in the first stage. Ergo, different upgrades were planned in order to gradually fulfil those parameters. The upgrades are going to be installed during a couple of long shutdowns (LS). Figure 2.2 shows the current schedule for upgrades and shutdowns at the LHC.
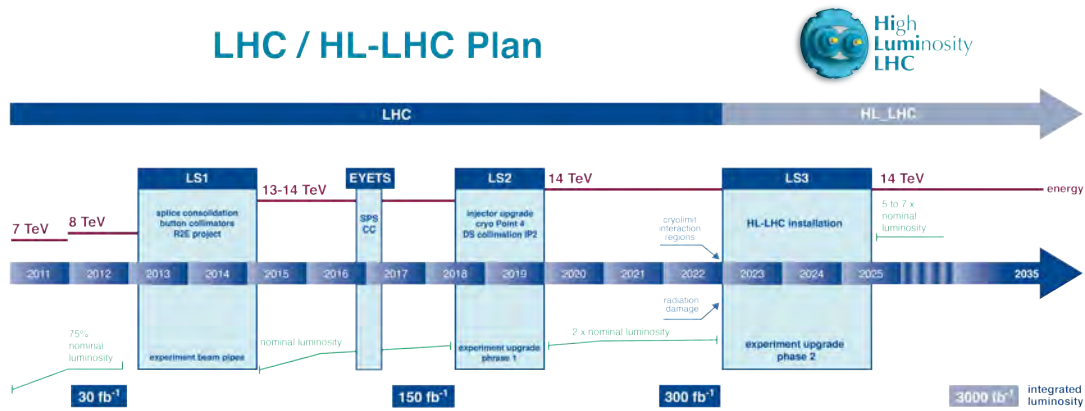
Figure 2.2.: Schedule of the LHC upgrades and runs [34].

After the end of LS1, the design-energy of the LHC will be available whereas the next two major upgrades will mainly improve the luminosity of the LHC. The result is the high luminosity LHC (HL-LHC). Some of the new challenges for the tracking detector will be:

- high fluences and the connected large radiation damages

- more events per interaction $\rightarrow$ higher trigger rate $\rightarrow$ more read-out speed required

- compensate lower precision of the tracker due to higher energy (compare Equation 1.6) with more distance between outermost layer and interaction point

Besides the requirements through the increased luminosity, the complete semiconductor pixel and stripe detector has to be replaced because of radiation damage resulting from previous runs and the new requirements. Hence, a new generation of pixel detectors has to be developed.

2.2. The ATLAS Detector

One of the main experiments at CERN is the ATLAS experiment [35] using the ATLAS general-purpose proton-proton detector. The ATLAS detector was built to exploit the full physics discovery potential of the LHC. In order to find new physics in a variety of fields, the detector provides as many signatures as possible including muon, jet, missing transverse energy, photon, electron and heavy flavour tagging. The variety of signatures is considered to be important to achieve potent and internally-verifiable data [36].
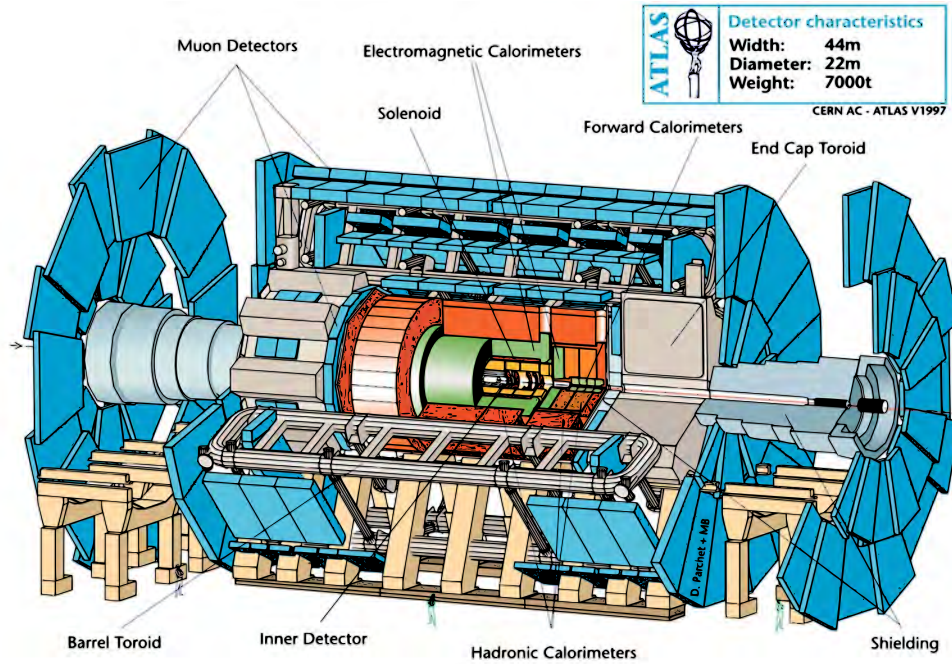
Figure 2.3.: Schematic view of the ATLAS detector with all main components [37].

2.2.1. Detector subsystems

The overall layout of the ATLAS detector is characteristical for a high energy physics experiment. The detector is roughly rotationally symmetric and consists of a central tracking detector close to the interaction point, situated in a 2 T solenoidal magnetic field. The next layer houses the electromagnetic and hadronic calorimeter as well as a second magnet which provides a toroidal magnetic field with a peak field of 3.9 T. The outermost parts are the muon chambers which provide high-resolution, large-acceptance and robust stand-alone muon spectrometry.

The Inner Detector

The Inner Detector is situated in a 2 T solenoidal magnetic field which is provided by a superconducting coil, cooled to 4.5 K with liquid helium using the calorimeter cryostat. The Inner Detector has a length of 7 m and a radius of 1.15 m. It provides momentum and vertex measurements as well as pattern recognition and enhanced electron identification. It consists of three parts:

- **pixel detector:** The Pixel Detector [38] has the best spatial resolution of all parts of the inner detector and is therefore installed as close as possible to the beampipe. Besides the three original pixel layers, an additional fourth layer (Insertable B Layer,

IBL [39]) was installed during the LS1. The planar sensor of the ATLAS pixel module has a pixel-size of $400{\times}50\,\mu m^2$ with a thickness of $250\,\mu m$. Each module has a size of $60.8{\times}16.4\,mm^2$ which results in 40960 pixel per sensor. The readout is done with the FE-I3 and always 16 Front-End (FE) chips were bump-bonded to one sensor chip.
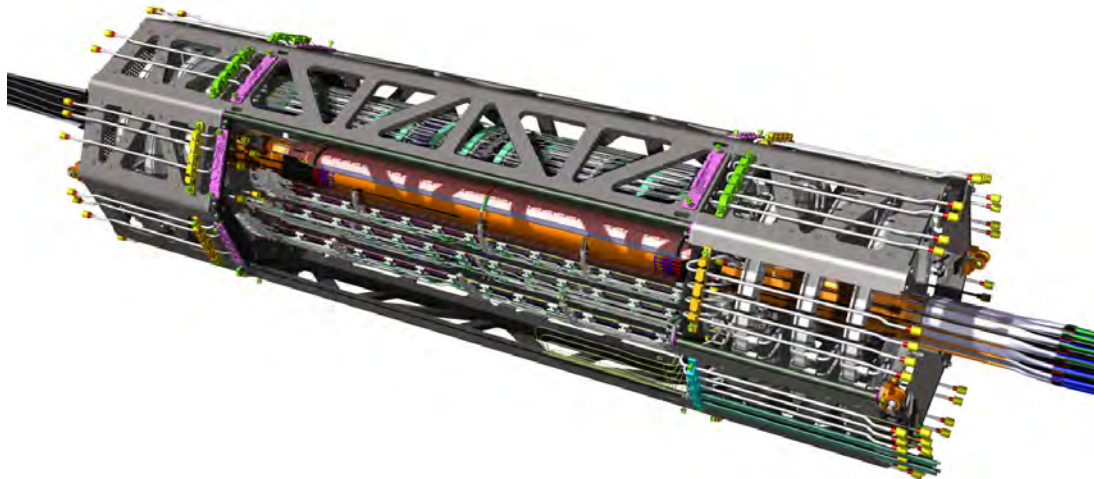
Figure 2.4.: Schematic view of the ATLAS pixel detector. Visible are the beampipe, IBL and the pixel detector [40].

The IBL uses two different sensor designs. One part of them are traditional planar sensors but the other part are so-called *3D sensors* (compare Section 3.2). Nevertheless, all of them have pixels with a size of $250{\times}50\,\mu m^2$. The planar sensors are bump-bonded to two readout chips whereas the 3D sensors fit to one FE. IBL uses a new FE chip, which is called FE-I4B. The motivation for IBL was to increase the resolution close to the interaction point in order to improve vertex and impact parameter reconstruction particularly for b-tagging. In addition, IBL will compensate irreparable failures of the current pixel detector caused by radiation damages [39].

- **Semiconductor Tracker (SCT):** The semiconductor strip detector [41] is the middle layer of the inner tracker. It consists of four concentric barrel layers and two end-caps of nine disks each. The geometry provides 4 points per track up to $|\eta| < 2.5$ [1]. In total 15552 silicon microstrip sensors are used in the experiment. All of them are $285\,\mu m$ thick and have 768 AC-coupled strips with a length of $123.2\,mm$.

---

[1]$\eta \equiv -\ln\left(\tan\left[\frac{\theta}{2}\right]\right)$, the pseudorapidity

The barrel module stripes have a pitch of 80 µm whereas the end-cap modules have a pitch of 57−94 µm.

The spatial resolution is 16 µm in rΦ-direction and 580 µm in z-direction.

- **Transition Radiation Tracker (TRT):** The outermost part of the inner detector is a transition radiation tracker [42]. It consists of three parts, a barrel and two end-caps with 52544 straws measuring 144 cm in length and 122880 straws measuring 37 cm in length, respectively. Its basic elements are thin-wall drift tubes (straws) which were chosen by cause of high modularity and because it is possible to implement an architecture where $35 − 40$ hits are guaranteed within a pseudorapidity of $|\eta| < 2$. The TRT improves the pattern recognition and it is mainly responsible for electron identification.

  The TRT-straws have an inner diameter of 4 mm which was chosen as good compromise between speed of response, number of ionisation clusters and mechanical as well as operational stability. They are operated in proportional mode with a gas mixture of 70% Xe, 27% CO_2 and 3% O_2. The 30 μm gold-plated tungsten anode wire is held at a voltage of 1530 V with respect to the straw wall. A single-point resolution of 170 µm in rΦ-direction is achieved [42].

The calorimeter system

Besides the tracking abilities of the inner detector, excellent knowledge of the individual particle-energy is necessary for high precision measurements. A good energy resolution as well as a linear energy response is important to determine the energy of particles over a wide range. The ATLAS calorimeter system is structured into an electromagnetic and a hadronic calorimeter.

- **electromagnetic calorimeter:** The electromagnetic calorimeter (EM) is a sampling calorimeter of lead absorbers (passive) and liquid argon (LAr) as active material [43]. LAr has the advantage of a very good intrinsic linear energy response and radiation tolerance. Furthermore, the EM has an accordion structure to provide extraordinary good hermicity and a behaviour for fast signal shaping which is required to cope with the 25 ns bunch-crossing interval of the LHC. The EM provides 24(26) radiation lengths in the barrel region and in the end-cap region, respectively.

  An energy-resolution of $\frac{\sigma_E}{E} = \frac{10\%}{\sqrt{E}} \oplus 0.4\% \oplus \frac{0.3\%}{E}$ is reached as indicated by test-beam measurements [44].

- **hadronic calorimeter:** The hadronic calorimeter [45] is also a sampling calorimeter. In account of different environmental behaviour of different positions in the

detector, different sampling calorimeters were chosen for the hadronic calorimeter. The less radiation harsh barrel region consists of iron absorbers and plastic scintillators whereas the more radiation harsh forward region uses again liquid argon as active material and copper as passive material.

The muon system

The muon spectrometer [46] consists of different tracking chambers. The barrel chambers are arranged in three cylindrical layers covering a pseudo-rapidity of $|\eta| < 1$ while the end-cap chambers ($|\eta| \leq 2.7$) are mounted on wheels normal to the detector axis. In total, the detector has a size of $44\,\text{m}$ in length and $22\,\text{m}$ in diameter. The muon system has two main functions:
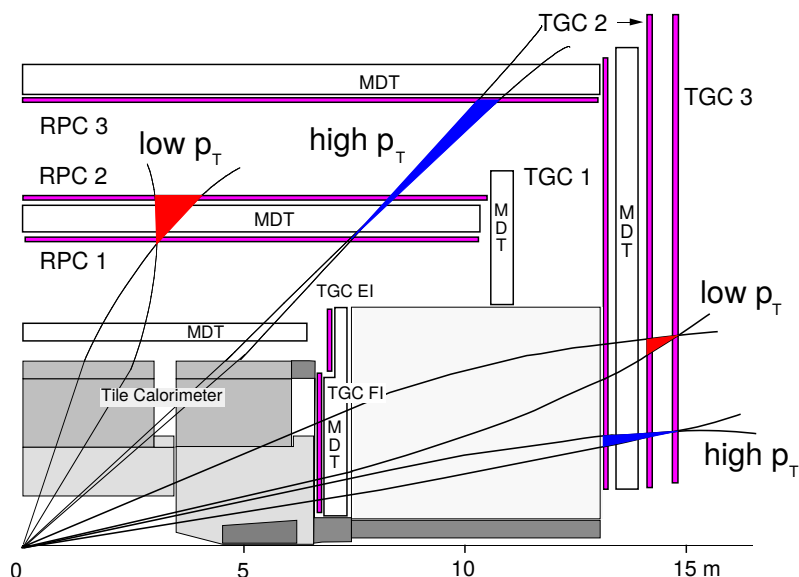
Figure 2.5.: Schematic view of the ATLAS muon spectrometer. Presented are the required coincidences for low-p_T and high-p_T triggers as well as the spatial arrangement of the detector components [46].

- **Trigger system:** Many interesting events contain muons. Therefore, a high p_T muon trigger was implemented in the ATLAS detector with two thresholds at 6 and $20\,\text{GeV/c}$ for muons pointing approximately to the interaction point. Two different detector technologies are used in the barrel and end-cap region according to the different requirements. In the barrel region, resistive plate chambers (RPCs) are used, whereas the end-cap region consists of thin gap (multi-wire) chambers (TGCs).

- **Precision measurements:** Besides the pure trigger information, a high momentum resolution is required. Therefore, a high track resolution is demanded. The requirements are fulfilled using monitored drift chambers (MDTs) and cathode strip chambers (CSCs).

Figure 2.5 demonstrates the composition of the muon spectrometer with the previously mentioned detector components.

3. Essentials of semiconductor pixel detectors

3.1. Essentials

The energy-band theory represents semiconductors with a valance and a conduction band. Both bands result from many discrete energy levels which are so closely spaced that they are considered as a continuum. Those energy levels arise from the periodic arrangement of the semiconductor atoms in the crystal lattice structure. Thereby, the electron wavefunctions overlap and form the pseudo-continuous energy bands [47].

Electrons are either bound to individual atoms (valance band) or they are moving freely in the atomic lattice (conduction band). Materials with an overlapping band structure or a small band gap (E_g <1 eV) are called conductors, typical semiconductors have a band gap of $E_g = 1-2$ eV and insulators have a band gap of E_g >4 eV. Consequently, semiconductor atoms are ionised with a small amount of energy resulting in temporary conductivity.

Typical pixel detectors are built out of semiconductors. The most used semiconductor is silicon due to the high availability and its wide spread in the semiconductor industry. The sensor of a pixel detector is usually built out of pure crystalline silicon which has different dopings (compare Section 3.2) in order to implement an efficient detection principle.

The electrical characteristics of a semiconductor are influenced by different dopings, which means the introduction of impurities into the crystal lattice. Two dopings are possible, the so-called *n-type* doping using donor impurities and *p-type* doping using acceptor impurities. For silicon, typical dopants are group III and V elements containing one valance electron less or more. Thus, acceptors need a silicon electron to bind into the lattice, leaving a hole as theoretical positive free charge carrier in the lattice. Donors have one valance electron more than needed to bind into the lattice which leaves a negative free charge carrier. Even though free charge carriers are released into the conduction band, the atoms are still electrically neutral. The more doping and the more impurities a semi-

conductor has, the lower gets its electrical resistance as more and more charge carriers are available for conduction. Besides the individual influence of both dopings, the combination of both types has an even larger influence on the functionality of the semiconductor. The interface between a p- and an n-type doped semiconductor is called pn-junction. Free charge carriers from both parts recombine in the border region, the depletion zone, namely the electrons from the n-doped region and the holes from the p-doped region. This process is driven by diffusion and works against the rising electrical field due to the imbalance of charge which is caused by the now ionised dopant. The n-type border region gets positively charged, meaning less electrons, while the p-type region gets negatively charged, which means more electrons. An equilibrium is reached when the force due to the electrical field is equal to the force due to diffusion. Then, no free charge carriers are left within the depletion zone. In order to collect the deposited charge of through-passing ionising particles, pixel detectors use an increased depletion zone produced by an external applied voltage in reverse bias. All produced charge carriers within the depletion zone get accelerated towards the p-type doped side for holes and the n-type doped side for electrons, respectively. Consequently, free charge carriers generated by ionising particles passing through the sensor drift towards the electrodes. A signal is generated at the electrodes as soon as charge carriers start movement, according to the Shockley-Ramo theorem [48] [49].

A pixel detector is a particle detector which is segmented in small discrete elements providing true 2-dimensional spatial information, which means it is not obtained by a combination of measurements. Every pixel detector consists of a sensor part where the signal is obtained and an electronics part which amplifies the signals and distinguishes signals from noise.

Pixel detectors are categorized into two classes. Hybrid pixel detectors consist of two individual chips. One part of it, the sensor, is built to collect the signal and the other part, the front-end, amplifies and processes the information, as indicated by Figure 3.1. Moreover, the front-end is used to transfer the obtained information from the individual pixel over the front-end chip through wires to the further read-out chain. This class of detector needs a connection between front-end and sensor. The demanding challenge is to connect all pixels of the front-end individually to the sensor. The small structures of each pixel demand high accuracy.

Usually, this is done with bump-bonds in a flip-chip process. With this process, the front-end is equipped with bump-bonds and the other part is flipped very precisely on it. High temperatures melt the bump-bonds in order to get a permanent connection between sensor and front-end. This process needs to be very accurate to place each bump-bond at the

exact correct position. Also the bond itself needs to be high-quality because all of them need to be completely equal to provide comparable connections all over the sensor. New approaches also try to establish a capacitive coupling between the two components. A very uniform layer of glue has to be applied on either the chip or the sensor before putting them together in order to hold them in position. Besides the advantage of a possible cost reduction using a much simpler process, the reduction of thermal stress for sensor and front-end is also not negligible. Nevertheless, a suitable, that means e.g. thermal stability, radiation hard glue has to be found and the alignment is even more important because of the missing self-alignment which is caused by internal forces from the bonds while bump-bonding.

The second class of pixel detectors are monolithic detectors, which combine sensor and read-out on one single chip. There are various concepts like DEPFET, MAPS, HV-CMOS and more. As a result of several restrictions, the electronic component is usually less complex compared to front-end chips of hybrid detectors. Furthermore, the read-out is usually slower than their hybrid opponents. The pulse detection is more efficient through the direct connection, even though monolithic sensors commonly have smaller depletion zones and thus smaller signals, the signal to noise ratio is mostly better compared to hybrid detectors.
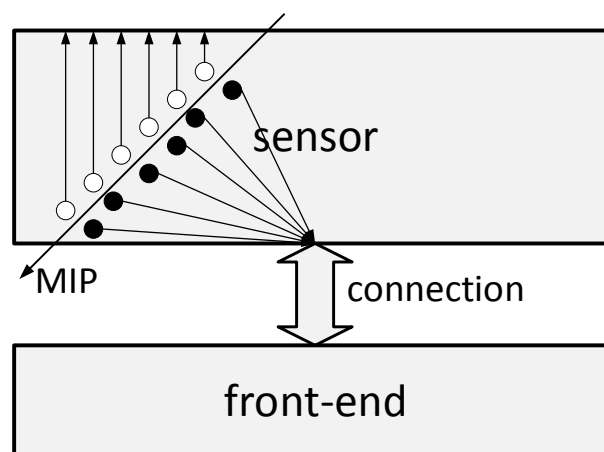
Figure 3.1.: Sketch of the construction of a hybrid pixel detector. The connection between sensor and front-end is realised with glue and a capacitive coupling or with bump-bonds and a direct connection. Black circles represent electrons and white balls represent holes.

3.2. Sensor concepts

The sensor part of a hybrid pixel detector collects the deposited charge whenever an ionising particle traverses the sensor. Different geometries, materials and processing techniques lead to different radiation-, noise and signal-development-behaviours. Consequently, the sensor-technology has a huge impact on the detector-performance. The most common sensor technology are planar sensors because of their comparatively simple structure and the established expertise about their construction and performance. New sensor technologies are being developed and analysed, but the required testing methods are developed and evaluated with planar sensors in this thesis due to the better understanding of their behaviour.

- **planar:** Usually, a planar sensor consists of a lowly doped substrate that is high-resistive with highly doped electrodes on both surfaces. One of the electrodes is placed on the bottom side to electrically connect the sensor and one of it on the top side which is segmented into a matrix forming the pixels. The applied reverse bias voltage between anode and cathode is typically chosen such that it depletes the whole sensor volume. Free charge carriers are directly separated and the drift due to the electrical field guides the electrons/holes to the electrodes. As a result of the complete depletion and a sensor thickness of typically $200-300\,\mu\mathrm{m}$, a large signal is observed (≈ 20000 e/h pairs for a MIP).
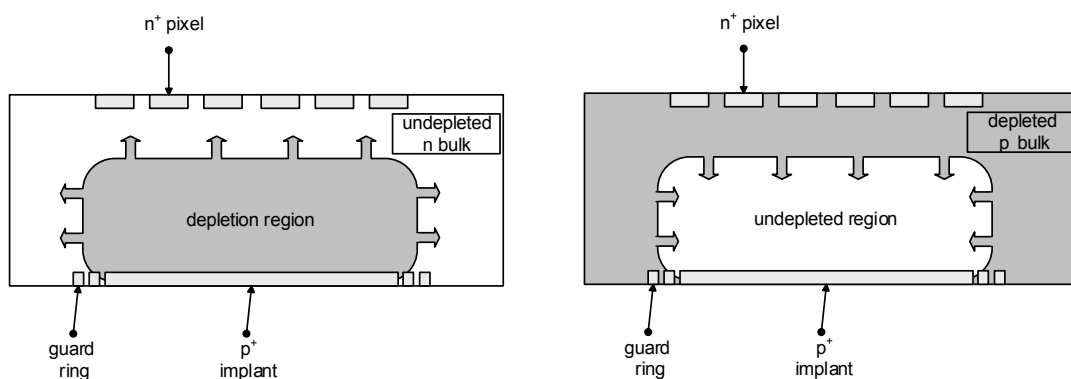
Figure 3.2.: Behaviour of an n^+-in-n sensor [50]. The left illustration shows an unirradiated sensor with a high-resistive n-doped bulk whereas the right illustration shows the same sensor after irradiation and type-inversion of the bulk.

Modern planar sensors are based on an n^+-in-n (or in-p) architecture, meaning that the substrate has a light n-doping and the pixels consist of highly n-doped material, whereas the contact electrode has a high p-doping and an additional metallization layer in order to electrically connect it. This has the advantage that the depletion zone of those sensors builds up from the back-contact (p^+ implant) to the pixels. The complete depletion is possible with low voltages ($\mathcal{O}(100\,\mathrm{V})$) because the sensor has a high resistance and a low doping concentration in this unirradiated state. The doping-type of the substrate changes during irradiation as the substrate always gets more p-doped during irradiation (type-inversion) and thus the depletion zone grows from the pixels to the back-contact and is consequently always present very close to the pixel where it is substantial for charge collection. In an irradiated state it is not possible to get a complete depletion as a result of radiation damages and the associated lower resistivity of the sensor. Nevertheless, this state is only reached after type-inversion where the depletion-zone grows from the pixels to the back-side which still guarantees signal collection at the pixels.

- **3D sensors**: 3D sensors have a 3 dimensional electrode layout. In contrast to planar sensors, holes are etched into the substrate of the sensor and filled up with the corresponding electrode material. This reduces the distance between the electrodes as well as the charge collection distance. Consequently, the required bias voltage is low before and after irradiation. Even more important is that the electrode spacing, prescribed through the desired charge collection efficiency and bias voltage after irradiation, can be independently chosen from the thickness of the sensor, defining the total generated charge per particle. An exemplary electrode layout of a 3D sensor is shown in Figure 3.3 .

3.3. Readout using a Front-End

Even though this thesis focuses on different sensor designs, the front-end part of a pixel detector is not less important. The following principles focus on front-ends for hybrid pixel detectors but they are generally also valid for the read-out chain of monolithic pixel detectors.

The following description of a front-end is based on the FE-I4 [51] front-end used for IBL and also for modules a and b (see Section 4.4 for details), investigated during this master thesis. The front-end consists of two main parts:
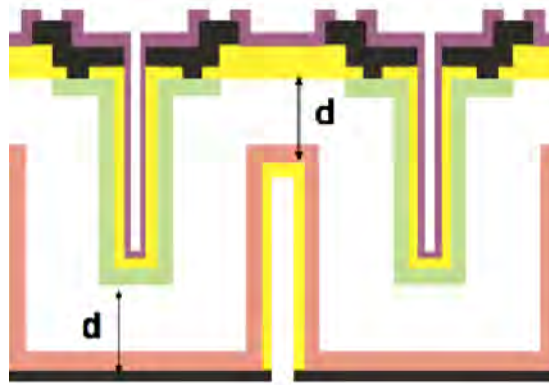
Figure 3.3.: Sketch of an electrode layout for a 3D sensor where the n^+ implantation is etched and filled from top and the p^+ implantation is etched and filled from bottom (double sided process) [39].

- **analog:** first, the analog part (see Figure 3.4) of the front-end handles the signal from the sensor. A preamplifier amplifies the signal in dependence on a global and a local tune-value. This value is used to compensate the influence of production fluctuations by changing a feedback current which is responsible for discharging the sensor signal. Also the leakage current of the sensor has to be compensated by a current which again acts at this point. Subsequently, a discriminator digitizes the
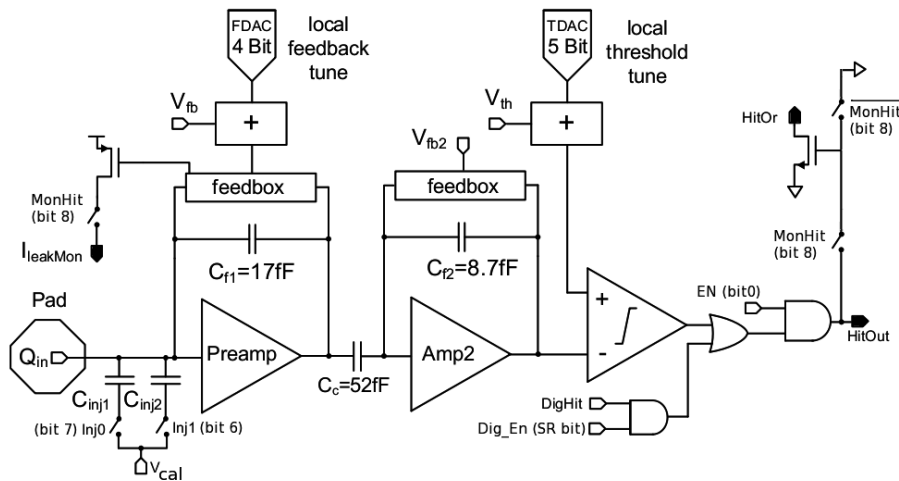
Figure 3.4.: Schematic view of the analog read-out part of the FE from the FE-I4B chip [51].

signal according to a global and a local tune value influencing the threshold. Besides the basic functionalities, the analog part contains an injection mechanism in order

to inject well-known amounts of charge into the circuit. The injection-mechanism is located between the sensor input-pad and the preamplifier, imitating real signals from the sensor.

- **digital:** the digital part analyses the signal and categorizes it into a time over threshold (ToT) code. This code provides information about the signal size as well as signals below the threshold. A ToT_{code} of 0 means one bunch crossing unit (BCU, 25 ns) over the threshold. This behaviour is valid for ToT_{code} values up to 13. ToT_{code} of 14 is an overflow bin and 15 means no hit.

  Then, further information processing is done on the chip like combining neighbouring hits and storing the data until a trigger initializes the read-out. Also, timewalk (compare Section 5.2 on page 50) is partly compensated in the digital part of the front-end by identifying small hits and relating them to coincident big hits (compare Section 3.4).

3.4. Timewalk

Timewalk describes the effect how small deposited charges are detected later compared to large charges. The effect is based on two components. There is a charge dependent part and a discriminator dependent part. The in-time efficiency is measured for different charges in order to evaluate the timewalk. The in-time efficiency describes the time-resolved hit efficiency of a pixel detector (compare Section 5.1).

Timewalk measurements are performed using the laser setup as well as the internal injection mechanism of the front-end. For the laser setup, in-time efficiency scans (see Section 5.1) are done for different laser intensities. There, the laser intensity is monitored using a photodiode (see Section 4.5.2) and the injected charge is calculated using the laser intensity calibration. Also, it is possible to use the ToT calibration (Section 4.5.5) in order to calculate the amount of injected charge according to the measured ToT. Furthermore, there is an internal timewalk measurement which uses the internal injection and delay mechanism. Nevertheless, the measurement principle is the same, the in-time efficiency is measured for different charges using the internal delay mechanism (T_0_scan). The injected charge is obtained using the VCAL-to-charge calibration (see Section 4.5.4). The result is for both principles the behaviour of the in-time efficiency's rising edge position relative to an arbitrary point in time (delay) against the injected charge.

The delay in this context is defined as the elapsed time between charge injection into

the sensor and firing of the pixel's discriminator. Firstly, the amount of injected charge is an important parameter. It influences the rising behaviour of the pre-amplifier and by this the delay. A smaller amount of charge leads to a smaller gradient and, consequently, the threshold of the discriminator is exceeded later (charge component) as it is shown in Figure 3.5. Besides the charge component, the *DisVbn* parameter determines the delay (discriminator component). It is an front-end configuration parameter and defines the current supplied to the discriminator [51]. Thereby, the discriminator speed is adjusted.
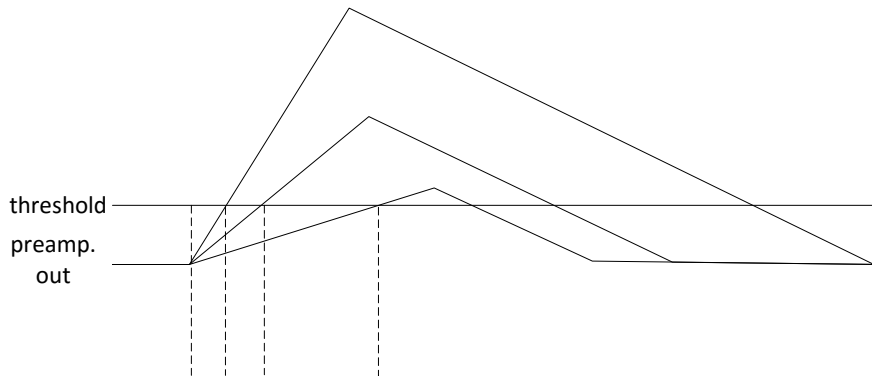
Figure 3.5.: Visualisation of the charge dependent component of the timewalk effect.

The amount of injected charge varies in the experiment from hit to hit. Moreover, it varies strongly between different adjacent pixel for one hit due to charge sharing. It is mandatory to assign every registered hit in the pixel detector to the corresponding interaction in order to be able to reconstruct the event afterwards. Unfortunately, a small charge deposition (small hit) may take up to 100 ns to be recognized whereas the response to a big charge deposition (big hit) may take just 50 ns. The exact timing for each charge is described by the timewalk which is why it is important to know it.

The FE-I4 can distinguish between small hits and large hits based on their ToT information. Hits with an ToT of 25, 50 or 75 ns (programmable) are classified as small hits, all ToT values above are classified as big hits. Particles passing through the sensor distribute their deposited charge over several adjacent pixels (cluster). Despite the charge sharing within the cluster, usually at least one pixel records a big hit. The ToT of this pixel is stored together with the ToT information of the neighbouring pixels in a shared memory block. Those surrounding hits tend to be small hits, hence they can not be assigned reliably to the appropriate bunch crossing. Therefore, the time stamp of the big hit is used for all hits within the cluster. As the delay saturates for large amounts of charge,

big hits are faithfully traced back to the proper bunch crossing. The linking of small hits with adjacent big hits makes it is also possible to associate small hits to the correct bunch crossing. Nevertheless, it is essential to know the exact timewalk behaviour of the pixel detector, for example in order to know which charge is sufficient for a reliable hit. Also, new module concepts can be classified using their timewalk behaviour.

3.5. DisVbn

The DisVbn parameter is a global register on the FE-I4, thus no per-pixel adjustments are possible. It controls the current supplied to the discriminator and influences its response-speed. To understand the impact of the discriminator current on its speed, one considers a model of an ideal discriminator, connected to an ideal inverter via a resistance and a capacity, as shown in Figure 3.6. The ideal amplifier outputs a voltage $V_{iaout} = g \cdot (V_{thr} - V_{pao})$,
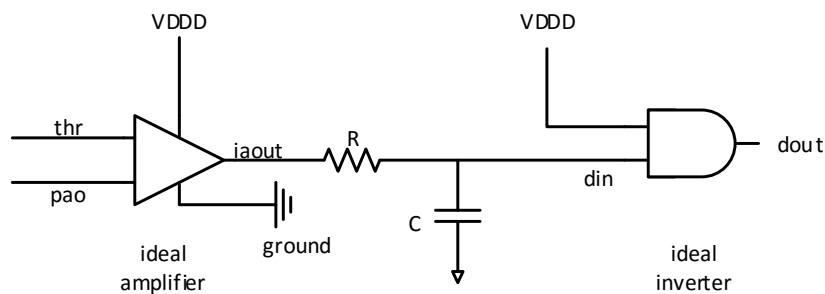
Figure 3.6.: Model of a discriminator based on an ideal amplifier and an ideal inverter connected via a resistor and a capacitor. *thr* is the adjustable threshold-voltage, *pao* is the pre-amplifier output, *VDDD* the digital supply voltage, *iaout* the ideal amplifier output, *din* the inverter input and *dout* the discriminator output.

where g is the gain of the amplifier. Nevertheless, the output voltage must stay between *ground* and *VDDD*. The output impedance of the amplifier is modelled via the resistor R (with voltage V_R) and the capacitor C (with voltage V_C) models the load capacitance of the ideal inverter.

Firstly, V_{pao} rises as a consequence of injected charge to the sensor. When V_{pao} exceeds V_{thr}, V_{iaout} rises quickly from *ground* to *VDDD*. The capacitor C begins to charge over the resistor R. Finally, the ideal inverter will begin to fire if the voltage across the capacitor exceeds a certain threshold V_{cthr}. The time it takes to charge the capacitor to

V_{cthr} depends on the current which is influenced via the resistance through the *DisVbn* parameter. This can be seen by setting up an differential equation for the model. V_C+V_R must be equal to V_{iaout} and V_C can be expressed as $\frac{q}{C}$. Moreover, V_R can be written as $R\dot{q}$ which results in

$$R\dot{q} + \frac{q}{C} = V_{iaout} \tag{3.1}$$

with the solution

$$q(t) = CV_{iaout}\left(1 - e^{-\frac{t}{RC}}\right) \tag{3.2}$$

which is plugged in into

$$V_C(t) = \frac{q}{C} = V_{iaout}\left(1 - e^{-\frac{t}{RC}}\right). \tag{3.3}$$

In order to get the time to charge the capacitor to V_{cthr}

$$V_C(t_{cthr}) = V_{cthr} = V_{iaout}\left(1 - e^{-\frac{t_{cthr}}{RC}}\right) \tag{3.4}$$

is solved for t_{cthr}

$$t_{cthr} = -RC \cdot \ln\left(1 - \frac{V_{cthr}}{V_{iaout}}\right). \tag{3.5}$$

Now *DisVbn* can be implemented in this model as an reverse influence on the resistor

$$t_{cthr} = -\frac{C}{DisVbn} \cdot \ln\left(1 - \frac{V_{cthr}}{V_{iaout}}\right). \tag{3.6}$$

Finally, it can be seen that *DisVbn* has an inverse impact on the delay, an infinite value of *DisVbn* results in a perfect and immediately responding discriminator. Consequently, the delay is then just given through the impact of different amounts of injected charge.

4. Measurement setup

The measurement setup was built in order to make high-precision space and time resolved efficiency measurements with different sensor concepts. A laser is used to inject charge into the sensor with high spatial and timing precision. The main components of the setup are the laser system and the Süss MicroTec PA300 probestation. The latter provides accurate positioning of the sensor and the beam-spot which is positioned by a movable microscope. The USBPix system is an interface board to digitally communicate with the read-out chip.

4.1. Probestation

The probestation [52] was built for wafer inspection, failure analysis and device characterisation of up to 300 mm diameter wafer. It consists of a movable chuck as well as a movable microscope above the chuck. Both are positioned with sub-micron accuracy. In order to increase the test capabilities of the probe station, a laser system was installed into the probestation to inject charge into a testing device. The testing device is placed on the chuck, which is positioned with a precision of $0.5\,\mu$m in $x - y$ direction and $0.25\,\mu$m in z direction. The microscope, which is used to guide the laser onto the sensor, is positioned with even higher precision: $0.25\,\mu$m in $x - y$ and $0.1\,\mu$m in z direction, respectively. Nevertheless, the actual spatial resolution is not as good as a result of additional uncertainties from the size of the beam spot. In order to provide stable thermal conditions, the temperature of the chuck is adjusted between $-55\,°$C and $160\,°$C. An EMI shield surrounds the chuck to eliminate electromagnetic interferences, improve thermal stability and provide a low light environment. Moreover, the case is combined with a safety interlock system to veto the laser in case of unclosed casing.

4.2. Laser system

The laser system Picosecond Injection Laser (PiLas) from Advanced Laser Diode Systems is used [53]. It is a pulsed laser with a built-in frequency generator for frequencies between

10 Hz and 1 MHz. Due to external triggering via USBPix, this feature was not used for any measurement of this thesis. The trigger pattern is a variable shape, rising edge trigger with a threshold of 0.2 V. The control unit, equipped with trigger in- and output, is connected to one of two available laser heads (671 nm and 1060 nm). Those laser heads are connected via optical fibres and an attenuator to the optical system of the microscope. The laser is used to inject charge into the sensor with high precision. Thereby, the charge injection is very flexible: the injection depth is varied by the wavelength of the laser, the amount of injected charge is controlled via the attenuator and the injection-position is set via the microscope and/or the chuck of the probestation. Even though two different lasers are available, only the 671 nm was used in this thesis.

4.2.1. Charge injection mechanism

The photons within a laser pulse ionise the atoms on the surface (absorption within a few nm) of the sensor. Moreover, it is also possible to inject charge deep (absorption within a few µm) into the sensor using the infrared 1060 nm laser. The used red laser has a wavelength of $\lambda =$ 671 nm, a pulse-width of 41 ps and a peak-power of 500 mW [53]. One photon has an energy of

$$E_{\text{photon}} = \frac{ch}{\lambda} = 1.848 \, \text{eV} \tag{4.1}$$

which is less than the typically needed energy to produce an electron hole pair in silicon ($W_{\text{silicon}} = 3.62 \, \text{eV}$). Therefore, multi-photon absorption is needed to produce free charge carriers in the bulk material.

   The aim of the laser injection is to simulate a minimal ionising particle (MIP) as it is the most frequent particle to be measured with the pixel detector in the real experiment. Nevertheless, the attenuator of the laser system is used to inject different charges. This can be seen by comparing the maximal amount of deposited energy of the laser

$$\begin{aligned} E_{\text{pulse}} &= P_{\text{pulse}} \cdot t_{\text{pulse}} \\ &= 500 \, \text{mW} \cdot 41 \, \text{ps} \cdot e \\ &= 128 \, \text{MeV} \end{aligned} \tag{4.2}$$

to the energy, needed to produce 20 000 e corresponding to a usual MIP signal, calculated by using Formula 1.3

$$E_{\text{MIP}} = 20000 \cdot W = 72.4 \, \text{keV}. \tag{4.3}$$

In order to calculate the injection depth, the absorption law is considered

$$\mathrm{I}(x) = \mathrm{I}_0 \cdot e^{-\mu x} \tag{4.4}$$

where $\mathrm{I}(x)$ is the intensity of the beam at a depth x with a starting intensity I_0. The material specific component μ is called absorption coefficient and was found in [54] for silicon at $300\,\mathrm{K}$. Consequently, the beam is reduced to 99% at a depth of

$$x_{99\%} = -\frac{\ln 0.99}{\mu} = 42.2\,\mathrm{nm} \qquad\qquad (670\,\mathrm{nm}) \tag{4.5}$$

$$x_{99\%} = -\frac{\ln 0.99}{\mu} = 6.1\,\mathrm{\mu m} \qquad\qquad (1060\,\mathrm{nm})\,. \tag{4.6}$$

4.2.2. Setup

A sketch of the laser setup is shown in Figure 4.1. The laser is guided by a single mode optical fibre through an attenuator. The attenuator consists of a lens constellation such that the Gaussian profile of the laser beam is not influenced while reducing the beam intensity by up to $40\,\mathrm{dB}$ [55]. The attenuation is controlled via a screw which is driven into the beam-line and thus reduces the beam intensity. The subsequent collimator then collimates the beam in order to feed the beam in the correct way into the further optical system on the probestation. The size of the beam-spot is minimised by matching the focal plane of the collimator with the focal plane of the microscope's lens tube using the screw on top of the collimator. A LINOS C-mount system connects the collimator with the beam splitter. Again, the length of the C-mount tube has to be adjusted very precisely in order to have the same focal plane at the beam splitter for the laser beam and the CCD image. Otherwise, the visible focus of the CCD image is displaced against the laser focus. The following 50/50 beam splitter then connects the collimator, the camera, the microscope and the photodiode (S9269) via the C-mount standard. Moreover, it splits the beam in order to measure the beam intensity with a photodiode while simultaneously illuminating the testing device. The camera is a Sony black and white CCD XC-ST50 CE with a resolution of 768×494 pixel [56] which is also illuminated through the beam splitter. Subsequently, a Mitutoyo FS70L THS microscope with four different magnifications focuses the beam on the sensor. A $2\times$, $10\times$, $20\times$ and a $50\times$ objective is available.
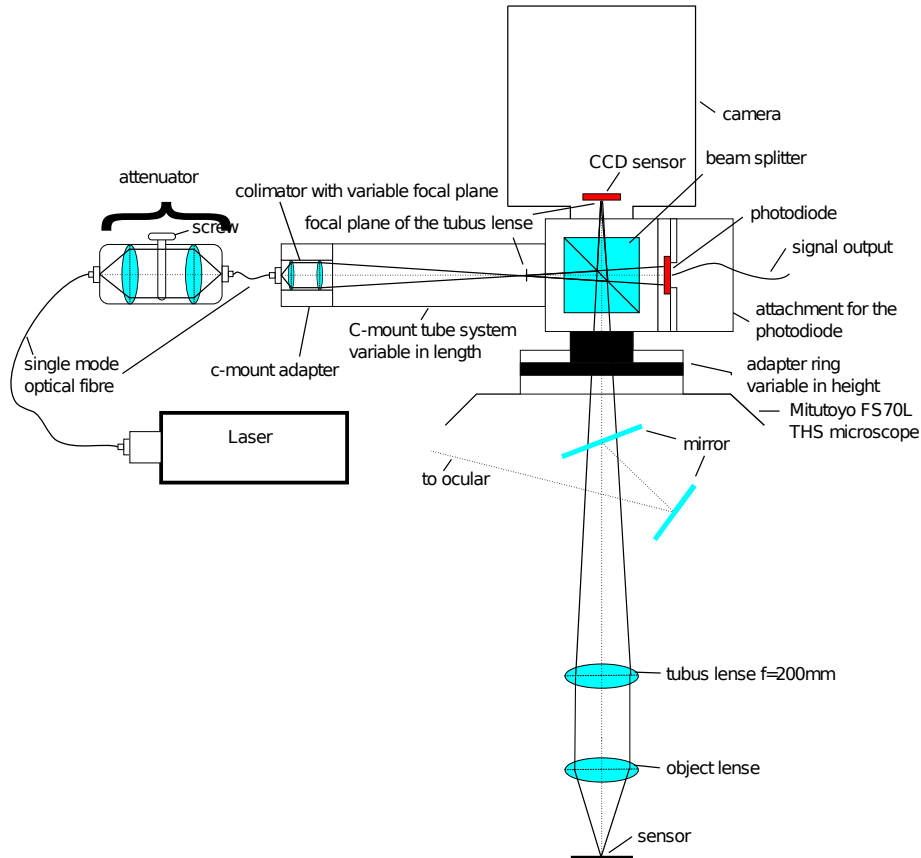
Figure 4.1.: Simplified view of the laser system setup [55].

4.3. USBPix and read-out

In order to compactly enable laboratory measurements with various possibilities to measure different signals and providing diverse voltages, the USBPix system was developed [57]. It consists of the Multi-IO board that is connected to an adapter card which is connected to the module card. The Multi-IO board is responsible for the communication to the PC as well as data acquisition and processing. Therefore, it has an Field Programmable Gate Array (FPGA), 16 Mbit SRAM and an USB 2.0 interface. Moreover, a micro controller handles the predefined scan routines which means that scan routines are executed without permanent communication to the PC. The LEMO connectors provide access to different signals of the Multi-IO board. One example is the strobe engine of the FPGA which is responsible for trigger signals and internal injections on the front-end. The adapter card and the module card are specific for different modules. It connects the Multi-IO board to the module card and also provides bias voltages to the module card. Three different adapter boards were used for this thesis. The FE-I4A/B Adapter Card is

used to connect one front-end of type FE-I4A/B. The Burn-in adapter card hosts up to four FE-I4A/B front-ends, either four Single Chip Cards, two Flex-Adapter Cards each containing two FE-I4B front-ends or one four-chip module. The last used adapter card was the Single Module Adapter Card which connects an FE-I3 to the Multi-IO Board. The module card hosts the module and is connected to it via wire bonds.

The software part of the laboratory read-out system is STcontrol, a C++ and ROOT based software application, based on the ATLAS PixLib package. It controls all types of scans and measurements and provides an Qt based user interface to configure and operate the connected assembly. Furthermore, it controls the microscope and the chuck in order to make efficiency scans at predefined positions.

4.4. Used Modules

Three different modules were used for the measurements of this thesis. The type and flavour-specific characteristics as well as the used adapter cards for all modules are presented here. The verification plots for all threshold and ToT measurements are shown in the appendix (Figure A.2, A.3 and A.4 on page 70). Table 4.1 summarizes the properties of all used modules.

Module	front-end	Threshold	ToT
a	FE-I4A	$(2910 \pm 40)\,\mathrm{e}$	$5.9 \pm 0.4 @ 20\,000\,\mathrm{e}$
b	FE-I4B	$(2827 \pm 97)\,\mathrm{e}$	$6.7 \pm 0.4 @ 20\,000\,\mathrm{e}$
c	FE-I3	$(2505 \pm 25)\,\mathrm{e}$	$29.1 \pm 0.9 @ 15\,000\,\mathrm{e}$

Table 4.1.: Summary of the properties of all used modules.

- **module A** consists of a 200 µm thick n-in-p sensor bump bonded to an FE-I4A read-out chip. The front-end was tuned to a threshold of 3000 e and to a ToT value of 6 at 20000 electrons which was both verified using a *Threshold_Scan* and a *ToT_verify* test of STControl. The module is mounted on a SingleChipCard Revision 1.1. The Adapter Board was an FE-I4A Adapter Card Revision 1.1a. The metallization on the top has two holes which allows laser injections with a wavelength in the visible spectrum. One of those holes is in the central part of the chip whereas the other one is in the top left part close to the edge (compare Figure 4.2).

- **module B** is an IBL production module: an FE-I4B read-out chip bump bonded to an n-in-n planar sensor (module name: S-10-3). The front-end was tuned to a
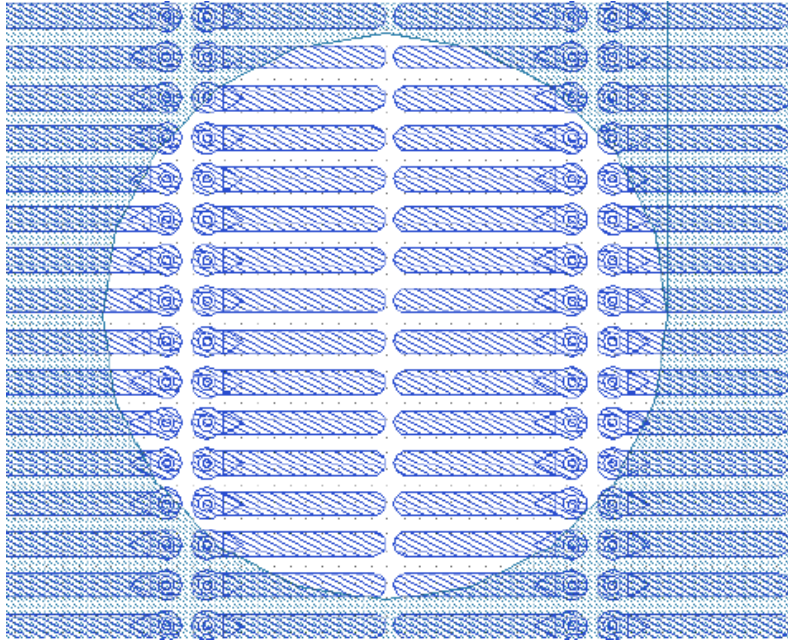
Figure 4.2.: Schematic view of the used central hole in the metallization of the surface of module A. Another rather similar hole is available in the edge region of the sensor [58].

threshold of 3000 e with a ToT value of 7 at 20000 electrons, again verified via a *Threshold_Scan* and a *ToT_verify* test. The adapter board is a Burn-in adapter card (Rev. 1.1) and the module is mounted on a Module Flex Adapter. This module consists of two front-ends, bump bonded to one double size sensor. A picture of the Module Flex Adapter and the Burn-in adapter card is shown in Figure 4.3.

- **module C** is an FE-I3 read out chip bump bonded to a planar sensor chip (module 11-5B). The front-end was tuned to a threshold of 2500 electrons with a ToT value of 30 at 15000 electrons, again verified via a *Threshold_Scan* and a *ToT_verify* test. The module is mounted on a Single Chip Card which was connected to USBPix via a Single Module Adapter Card Rev. 1.0. A picture of the Single Module Adapter Card and the Single Chip Card is shown in Figure 4.4.
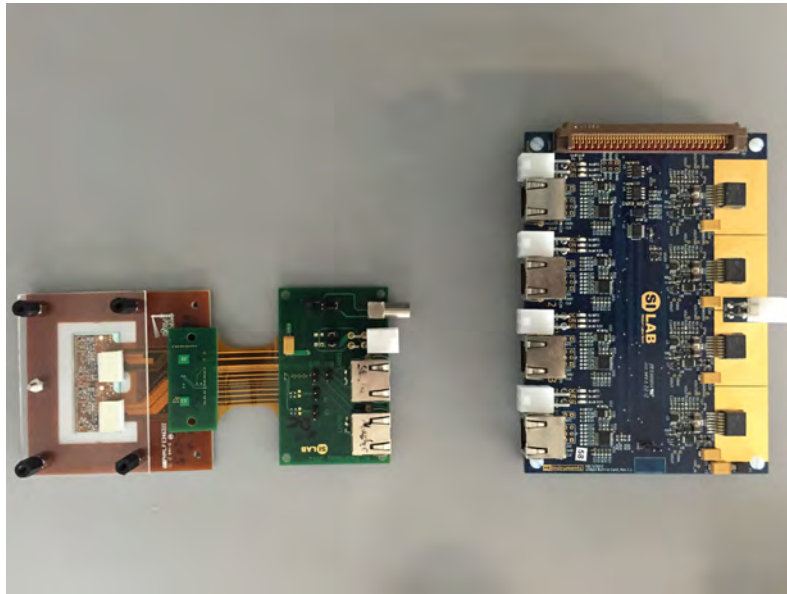
Figure 4.3.: Module B mounted on the flex adapter (left part) and the Burn-in adapter card (right part) which connects the module to the Multi-IO Board.
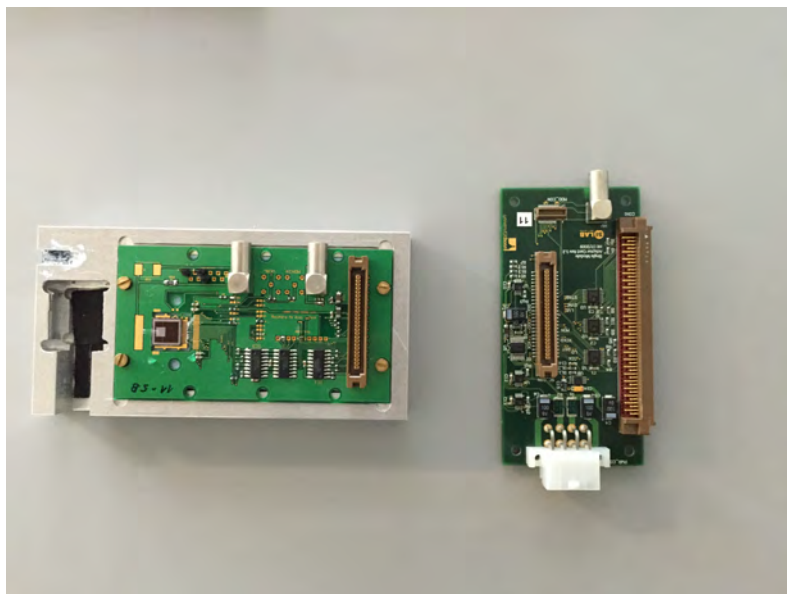
Figure 4.4.: Module C mounted on the Single Chip Card (SCC, left part) and the Single Module Adapter Card (right part) to connect the SCC to the Multi-IO Board. Furthermore, the SCC is mounted on a support structure to ensure good contact with the surface of the chuck in the probestation.

4.5. Calibration

4.5.1. Laser dimensions

One of the most important information about the laser setup is the size of the beam-spot. On the one hand, it is important to set a scale for the step size of all spatially resolved measurements. On the other hand, for time-resolved hit efficiency measurements it should be ensured that the laser deposits its complete power just within one pixel. The laser-size was measured with module A. The hole in the top-layer metallization was used to inject charge with the laser.

The laser was sampled over the edge of the metallization onto the bare substrate directly in the middle of a pixel. Thus, the hit detection probability is given through a step-function, 0 on the metallization and 1 on the substrate. The mean ToT for 1000 injections at each position results in a sigmoid function. It is theoretically given through a convolution of the width of the beam-spot and the ToT-to-charge calibration function, which is known. Consequently, the width of the laser is obtained by a fit of a sigmoid function, where a Gaussian beam profile is assumed. The result of one scan is shown in Figure 4.5. The measurement was repeated for different z-positions in order to identify the beam divergence and the focus-plane. The result is shown in Figure 4.6.

The beam is less divergent for smaller magnification. Nevertheless, the beam divergence is small over all magnifications but the focal point changes for different magnifications. This effect can be explained with a not perfectly aligned optical system but it was compensated by repositioning the microscope for different magnifications. In order to deposit a major fraction of the beam energy in a known area at least a 2-σ interval (containing 90.25% of the beam pulse) is required. A minimal spot size (1-σ) of about 1 µm leads to a meaningful grid-size of 5 µm considering a factor of 2 for a 2-σ interval and another factor of 2 for the beam-diameter not the beam-radius given by the standard-deviation. Furthermore, the beam-pulse reliably deposits its complete energy within one pixel which can be seen by comparing the pixel size of at least 50 µm.

4.5.2. Laser intensity

In order to monitor the laser intensity, the photodiode which is coupled to the beam via the beam splitter is used. Therefore, two steps are necessary: firstly the ToT-to-charge calibration is obtained for module C. Then, the voltage of the photodiode is calibrated to
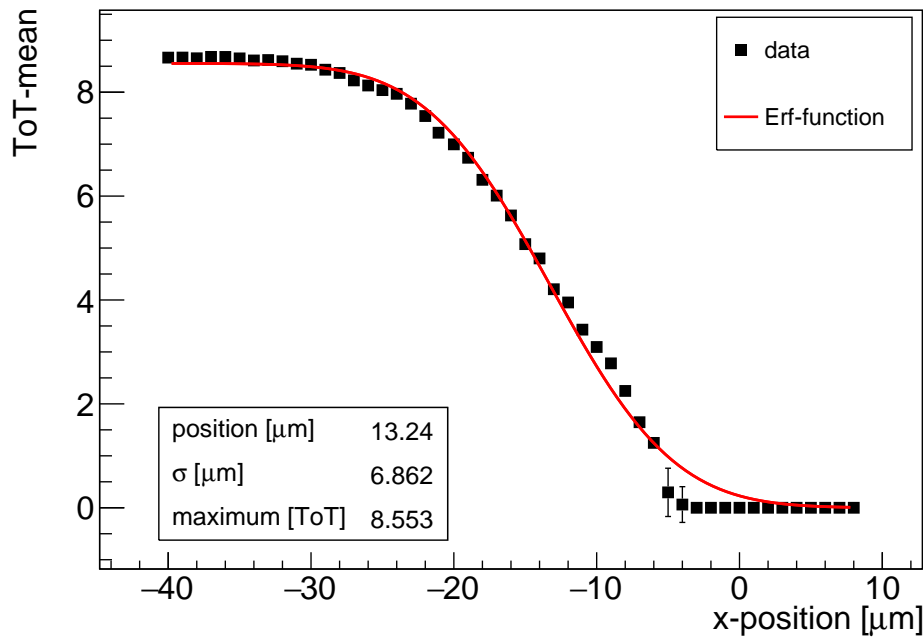
Figure 4.5.: Exemplary ToT turn-on curve for a magnification of 50 at a height of $z+50\,\mu m$, where z is the optical focus height. The mismatch between fit and data in the low ToT regime (0-1) is due to the non-zero threshold which is not included in the model of the fit-function.

the charge measured by the pixel-module for various laser intensities. Module C was used for this calibration because the ToT information of FE-I3 has 8 bit whereas FE-I4 has just 4 bit and the spectroscopic properties are essential for this calibration. Even though there were major changes to the front-end from version 3 to 4, the injection mechanism is almost similar. STControl and USBPix are still used[1], only the adapter board has to be changed to a Single Module Adapter Card (compare Section 4.3 on page 32).

ToT-to-charge calibration

Two capacitors are available (C_{low} and C_{high}) in the injection circuit of the front-end and after charging them with a voltage defined by a DAC value, their (one or both) charge is injected into the read-out circuit. To get the ToT-to-charge calibration three steps have to be done. The DAC steps of the internal injection mechanism are mapped to a voltage. Then, the capacity of the injection capacitors is measured. Finally, the ToT-to-DAC behaviour is obtained using an STControl built-in scan (*ToT_Calib* scan).

---

[1]software/firmware in different versions
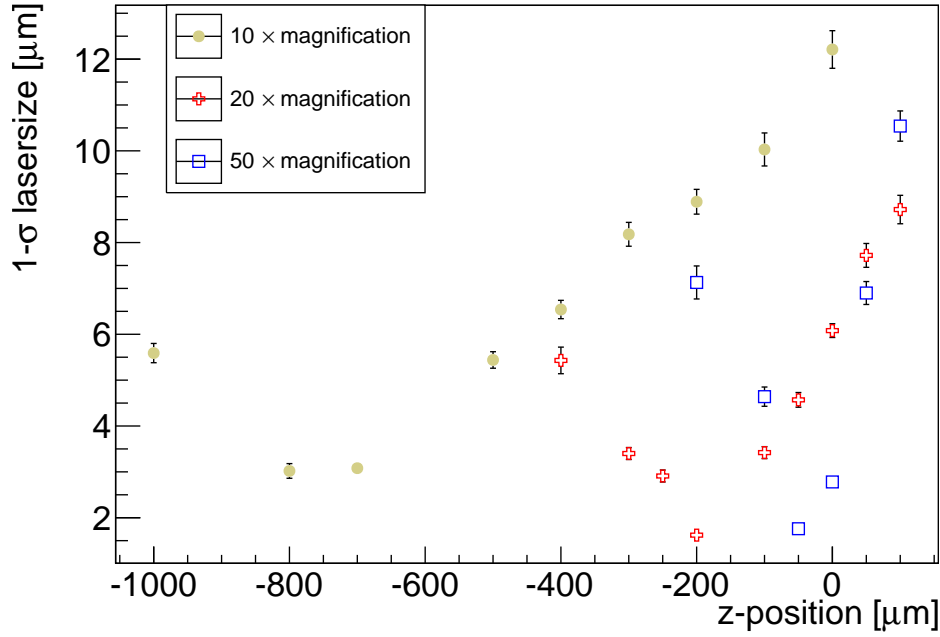
Figure 4.6.: 1-σ radius of the beam-spot using different magnifications. The z=0 position is found by optical focussing the camera image.

To begin with, the VCAL (DAC) to voltage behaviour is measured. The VCAL value defines the voltage which is applied to the injection capacitors. The actual step-size is obtained by using different VCAL values while simultaneously measuring its output voltage on the single chip board.

Each capacitance is internally connected to a square wave signal with a frequency relative to the base frequency of 40 MHz. There, the base frequency is devided by a factor between 4 and 32 and additionally the multiplicity of the capacity itself is chosen to be 0×, 1×, 2× or 4×, respectively. Then, a known voltage (U=2.28 V) is applied through a current meter to the capacitors such that voltage and current are known. Consequently, the current is measured as a function of the applied frequency. It is valid that

$$\frac{U}{I}\sin(\phi) = \frac{1}{fC} \tag{4.7}$$

$$\Rightarrow I = UCF = k \cdot f \tag{4.8}$$

where k is the slope of the fits in Figure 4.7. The capacity of the capacitors then is calculated to be

$$C = \frac{k}{U}. \tag{4.9}$$

The $0\times$ measurement is used to identify and subtract stray capacities. The capacitances
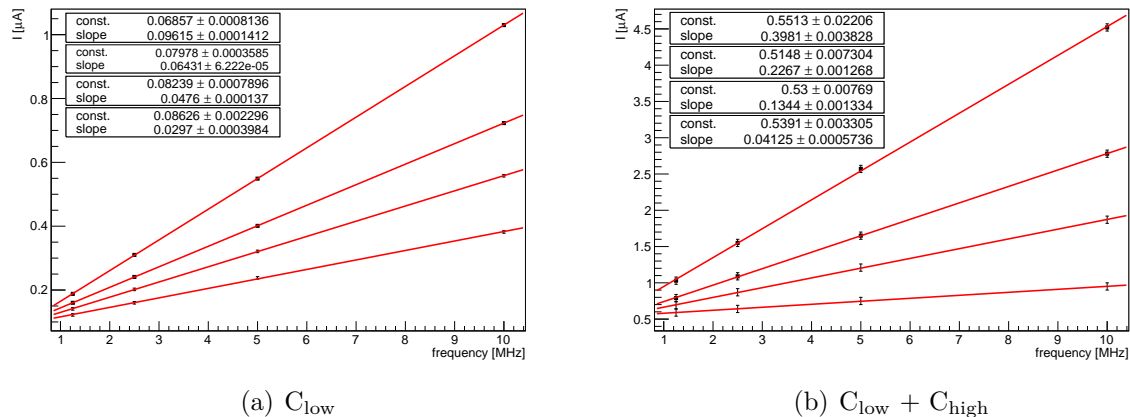
(a) C_{low} (b) $C_{low} + C_{high}$

Figure 4.7.: Behaviour of the current through (a) C_{low} and (b) $C_{low} + C_{high}$ for different applied frequencies. For both capacities all four multiplicities were measured. The top most dataset corresponds to the $4\times$ measurement and the lowest one to the $0\times$ measurement.

are $C_{low} = (7.58 \pm 0.08)\,\text{fF}$ and $C_{high} = (32.6 \pm 0.4)\,\text{fF}$.

The next step is to measure the ToT-to-VCAL behaviour. Therefore, STControl provides the *ToT_Calib* scan which varies the charge injection via different VCAL values. Additionally, the measurement is done one time using C_{low} and one time using C_{high} (see Figure 4.8 (a) and (b)).

The VCAL values are transformed into a voltage using the first calibration. Then, the voltage is again transformed into charge using the capacity which was determined in step two. This leads to the final ToT-to-charge calibration which is shown in Figure 4.8 (c) and (d).

Photodiode calibration

In the next step, the voltage of the photodiode (U_{pin}) is measured for different intensities of the laser. Therefore, the intensity is varied while the ToT spectrum is recorded for

(a) C_{low}

(b) C_{high}

(c) C_{low}

(d) C_{high}
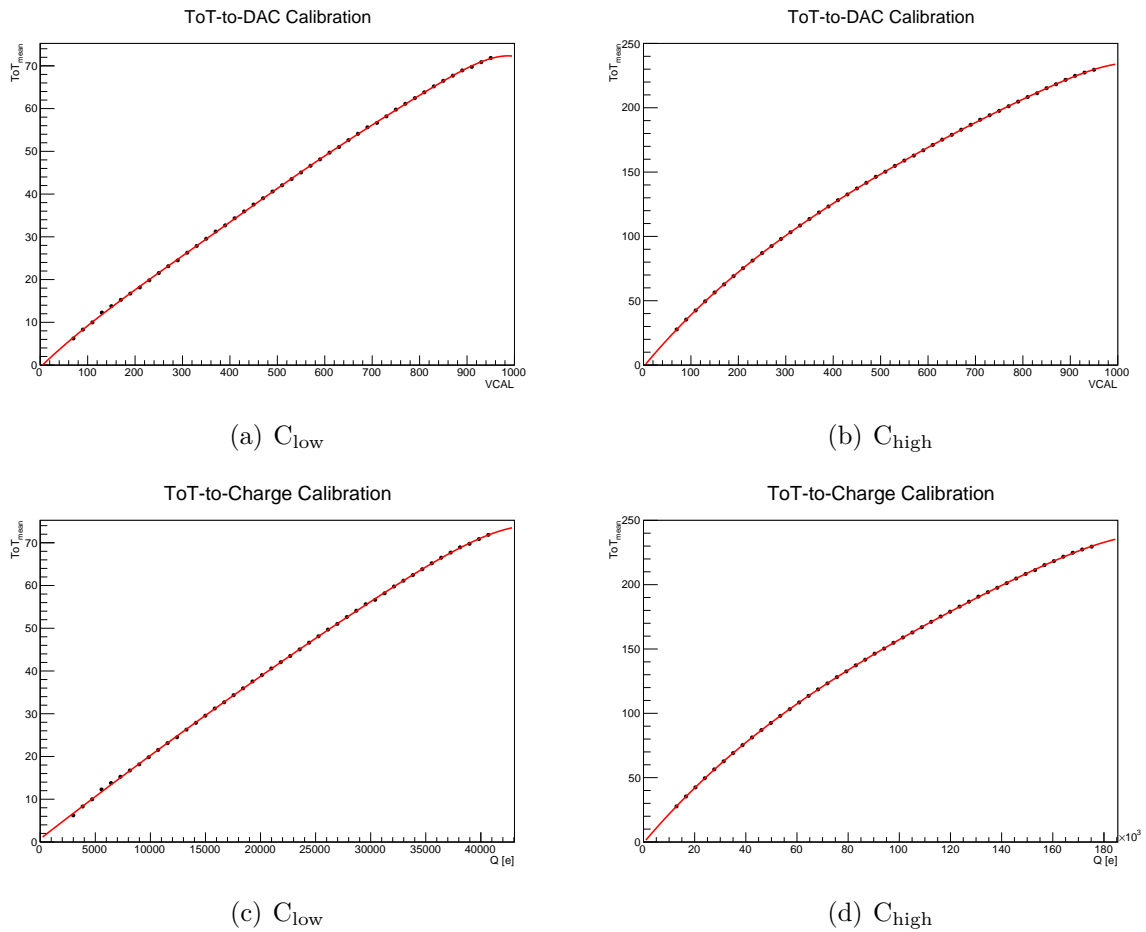
Figure 4.8.: ToT-to-charge calibration for module C using the VCAL-to-voltage and capacity determination of the previous steps. Figure (a) and (b) show the original data (ToT-to-DAC) whereas Figure (c) and (d) show the transformed x-axis into charge. The data was fitted with a third order polynomial.

each intensity. With help of the ToT-to-charge calibration of the previous section, the ToT spectra are transformed into charge spectra. In order to get the pin-diode voltage to charge calibration, the mean value of these charge spectra are plotted against the pin-diode voltage in Figure 4.9. Additionally, a third order polynomial is fitted, the result is also given in the plot.

The voltage of the photodiode strongly depends on the laser frequency [55]. Usually, the laser is driven with a constant frequency but for all later measurements an external trigger of USBPix is used. Consequently, the same conditions have to be simulated during the calibration. There are several read-out breaks of the measurement at several points of a scan which also effects the behaviour of the laser. Therefore, the calibration is done
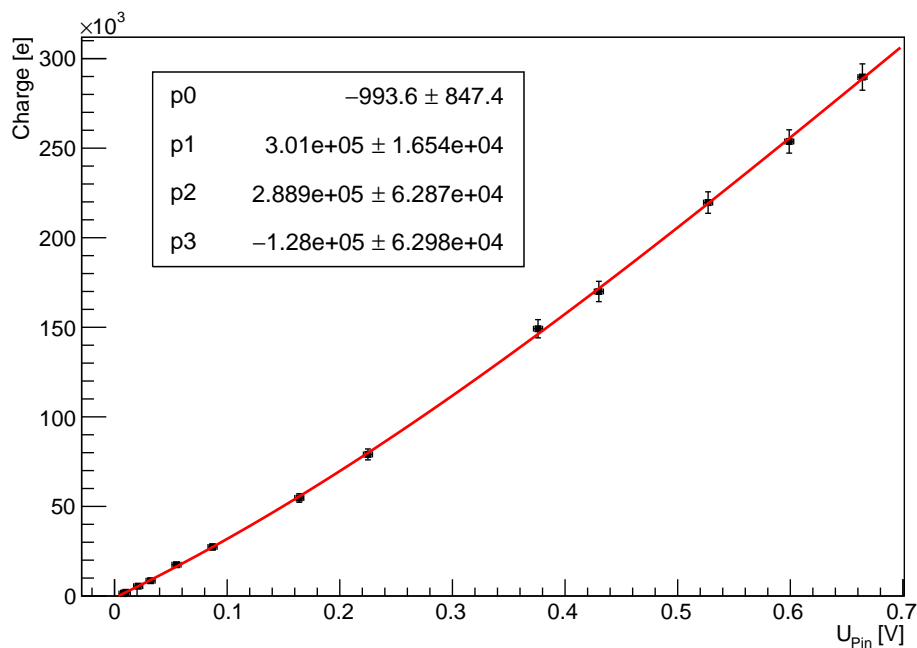
Figure 4.9.: U_{pin}-to-charge calibration. The data was fitted with a third order polynomial. The error in *y*-direction include systematic errors due to the VCAL-to-voltage calibration.

using a parallel setup[2] in order to trigger the laser with the appropriate frequency while recording the data with module C. Any change in the trigger frequency causes major effects on the calibration. Thus, no changes were applied to the strobe engine[3] frequency and duration configuration for all modules during any scan.

4.5.3. Laser delay

A high-resolution delay mechanism was implemented into the USBPix firmware in order to delay the output of the internal strobe engine. This feature is used by all laser timing measurements - the strobe engine triggers the laser through an output of the Multi-IO board. The delay mechanism uses a parameter called *Strobe_fine_delay*. It needs to be calibrated in order to trace-back from the parameter to the actual time in SI units.

The relative delay is shown as a function of *Strobe_fine_delay* in Figure 4.10. *Strobe_fine_delay* is just defined up to values below 2000. Above this value, it starts from the beginning.

---

[2]a setup of module A was used as the parallel setup
[3]used for triggering the laser

Despite the fine step size of $(24.4 \pm 0.2)\,\mathrm{ps}$, the full range covers more than $48\,\mathrm{ns}$ and consequently almost two complete bunch crossings ($2{\times}25\,\mathrm{ns}{=}50\,\mathrm{ns}$).
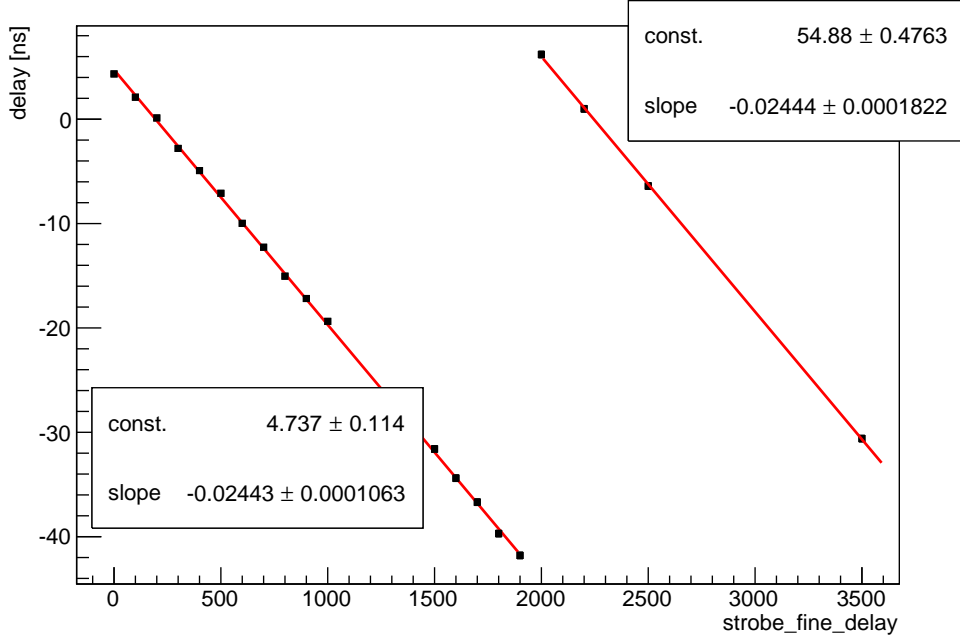
Figure 4.10.: Calibration of the delay mechanism for the laser trigger. The fit function is a first order polynomial. The error bars are to small to be seen.

4.5.4. VCAL-to-charge calibration FE-I4

This VCAL-to-charge calibration is needed in order to evaluate all measurements with module A and B in terms of charge. Especially, it is used for the internal timewalk measurements of module A. In order to infer back from the VCAL DAC values (*PlsrDAC*) to the injected charge, the injection voltage is measured for different DAC values. The injected charge is then given by

$$Q_{\mathrm{inj}} = C_{\mathrm{inj}} \cdot (PlsrDAC \cdot a + b) \qquad (4.10)$$

where C_{inj} is the injection capacitor, a the gradient of the VCAL to voltage calibration curve, and b the charge injection offset. The measured values are shown in Figure 4.11 and a fit of a first order polynomial results in a gradient of $(1.413 \pm 0.001)\,\mathrm{mV}/PlsrDAC$ in the central region. The offset was determined separately with an *Injection Calibration*

Scan [59]. The result is an offset of 12.78 mV.
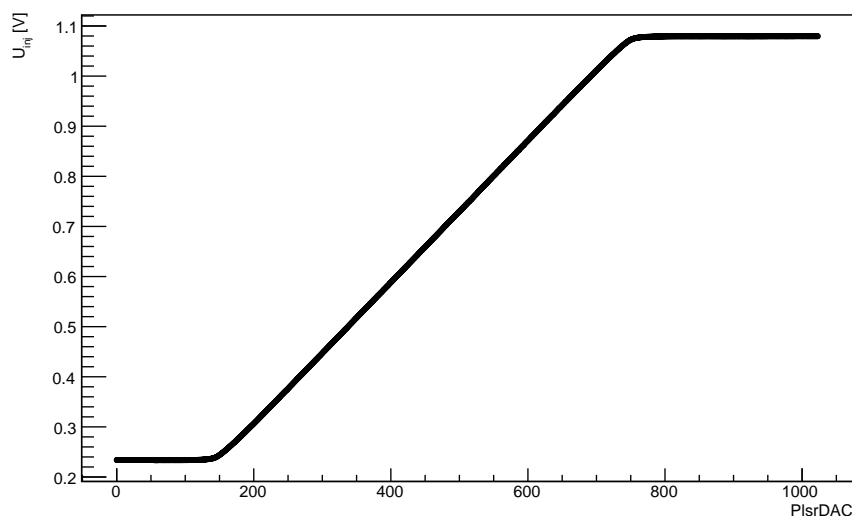
Figure 4.11.: Measurement of the injection voltage for different *PlsrDAC* values of module A.

4.5.5. ToT calibration FE-I4

A *ToT_calib_alt* [59] scan was performed to measure the ToT behaviour for different VCAL values. The calibration was done by determining the mean ToT values for each DAC value. The VCAL-to-ToT calibration varies between different pixels due to manufacturing margins. Therefore, the calibration was done for the pixel[4] which is later used for timewalk measurements with the laser setup. Figure 4.12 shows the behaviour of ToT against VCAL for this pixel. In combination with the VCAL-to-charge calibration of Section 4.5.4, another approach to calculate the injected charge for laser measurements is available.

4.6. Measurement assembly

The main measurements (in-time and spatially resolved hit efficiency) were done using the following setup. It uses the USBPix system for triggering and control. Trigger information is provided to the laser system using the strobe engine of USBPix. Therefore, the TX[2] output is connected to the Trig-In input of the laser (via a Lemo cable). Also, the

---

[4]module A: column 35, row 167
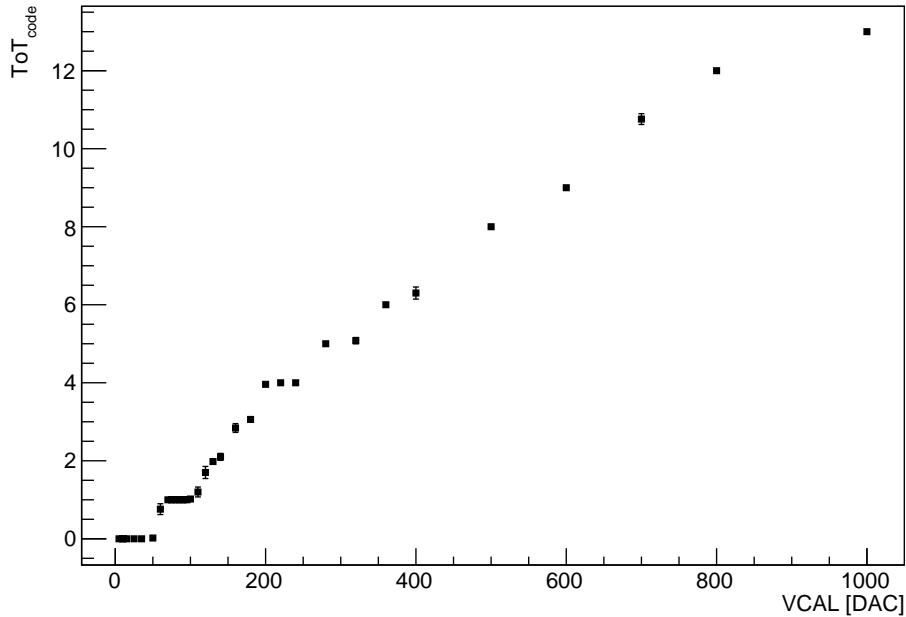
Figure 4.12.: VCAL-to-ToT calibration of module A, pixel 35/167. The ToT_code values
are mean values for 50 injections per point.

read-out of the front-end is triggered by USBPix. The bias voltage is chosen to be 80 V
for module A and C and 100 V for module B. A schematic view of the setup is shown in
Figure 4.13 and Figure 4.14 shows a picture of the setup for module A.

The timing of the external trigger is controlled very precisely via the *Strobe_fine_ delay*
parameter with a step-size $\Delta t <$ 25 ps. Nevertheless, another delay mechanism (*Strobe_delay*
parameter) is needed for internal injections. It has a much broader step-size of about 1 ns
using the default configuration[5].

---

[5]the step-size is tuneable, see Section 5.3 on page 53 for details
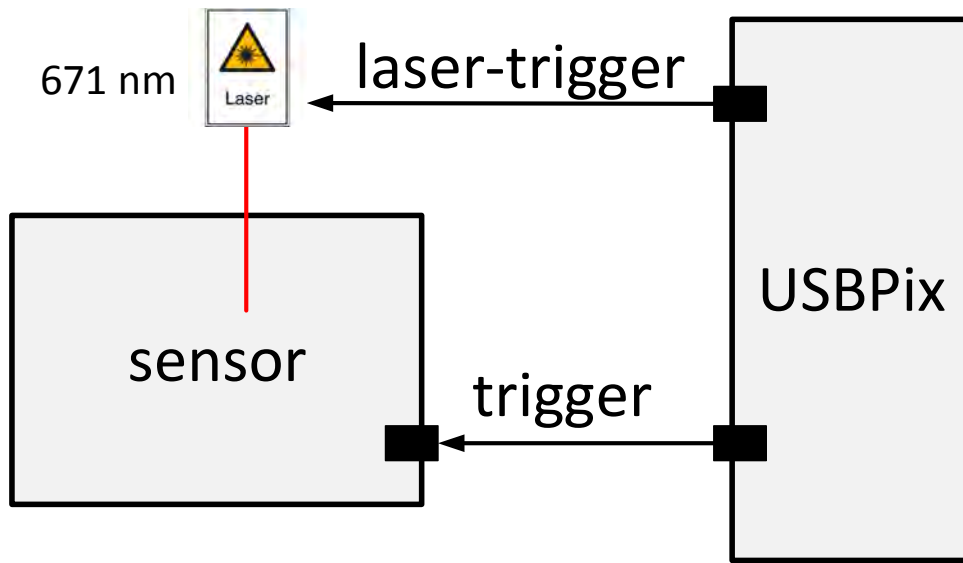
Figure 4.13.: Sketch of the measurement setup. USBPix controls the complete timing of the laser and the read-out trigger.
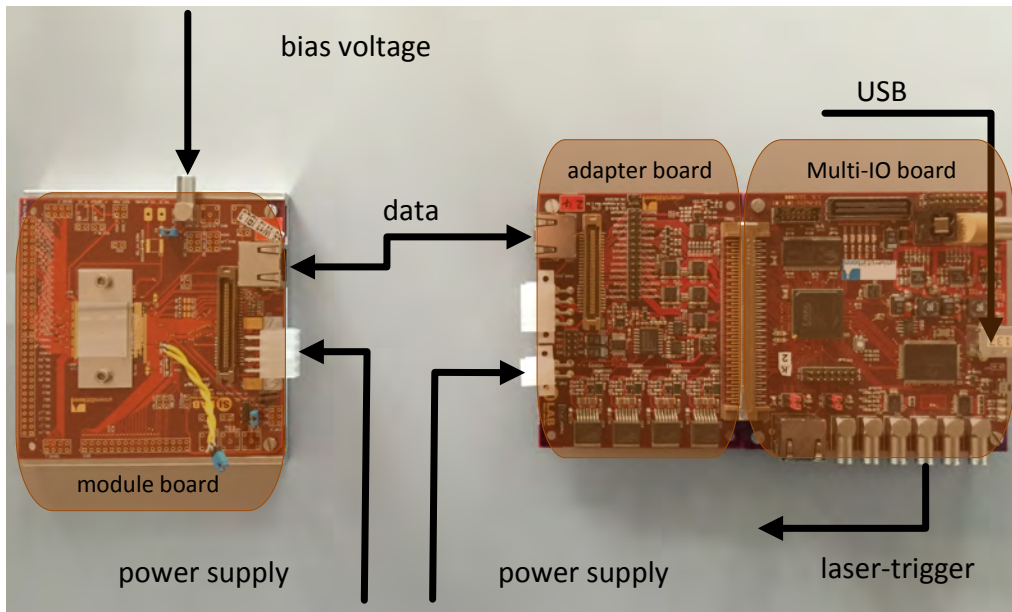
Figure 4.14.: Picture of the USBPix read-out system with module A and adapter card as well as the Multi-IO board.

4. Measurement setup

5. Time-resolved hit efficiency measurements

The LHC beam collision frequency is 40 MHz corresponding to a bunch crossing every 25 ns. The challenge is to refer each hit in the pixel-detector to the corresponding bunch crossing. Therefore, the LHC beam clock is also provided to the pixel detector. Nevertheless, various noise sources lead to a jitter of all signals inside the modules which in turn influence the recorded time of an event. Timewalk also shifts the detection-time by an unknown factor into the past. Altogether, there are multiple reasons for a timing mismatch resulting in a degradation of the overall efficiency. Thus, it is very important to know the time-resolved hit efficiency as well as the timewalk behaviour of a detector to provide appropriate timing information.

5.1. In-time efficiency

The in-time efficiency describes the time-resolved hit efficiency of a pixel detector. Figure 5.1 describes all important signals during a measurement. All signals on the front-end are measured at the rising edge of the LHC beam clock (clock). The laser system is triggered via the strobe signal generated within the Multi-IO board (laser-trigger). The produced laser-pulse releases charge carriers which are collected and generate a signal in the pre-amplifier of the front-end. Subsequently, the discriminator output is high from the moment the threshold is exceeded until the preamplifier-output signal falls below threshold. The ToT information is stored in the hit buffer together with the hit-time information. After a predefined time (trigger delay) a read-out trigger is sent from US-BPix to the front-end. The trigger delay is controlled by STControl. The delay mimics the time which is needed in the real experiment to generate a trigger signal based on the information of other detector components. The trigger requests the hit information on hits registered a predefined time before (latency). The stored hit then has to be within a time acceptance window, which ideally is one clock period.

The measurement of the in-time efficiency is realised by delaying the laser trigger. This
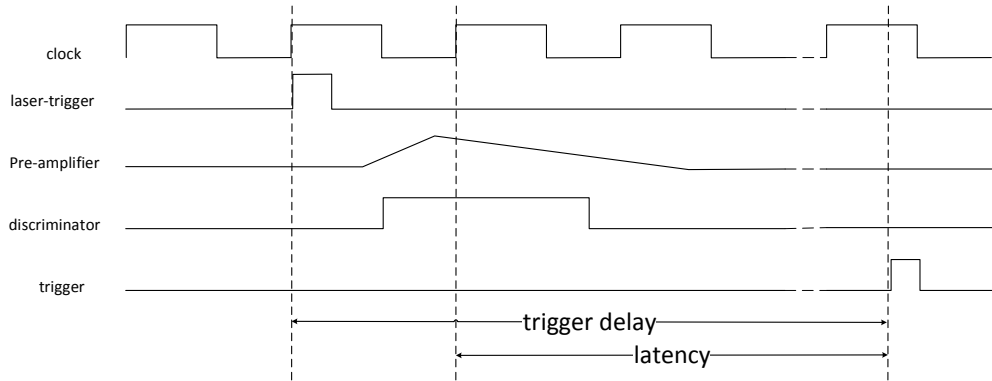
Figure 5.1.: Signals within the system. A measurement starts with the laser-trigger which causes a laser-pulse. The deposited charge is amplified by the pream-plifier and digitised by the discriminator. Finally, the read-out trigger requests data within the shown time window.

means that there is a fixed point in time for the read-out trigger but all other remaining signals depend on the delay of the laser-trigger. Consequently, the acceptance window is sampled by the hit occurrence. Finally, the occupancy results in a box-shaped function with smeared edges caused by signal jitter and module specific characteristics. This module design-dependence enables the in-time efficiency to be a figure of merit for module concept studies.

Figure 5.2 shows the correct timing whereas Figure 5.3 shows the behaviour when the timing is incorrect and the hit occurs not within the acceptance window. Such hits are not counted and the efficiency decreases.

In-time efficiency measurements were performed with module A and the result is shown in Figure 5.4. The laser attenuator was configured to obtain a laser-pulse leading to a charge injection corresponding to a ToT value of 9. Thus, a really large charge ($\gg 20000\,\mathrm{e}$) was used in order to avoid charge-limited effects and therefore the maximal in-time efficiency is obtained.

Theoretically, one clock period has a length of $25\,\mathrm{ns}$. The measured full width at half maximum (FWHM) of the in-time efficiency of $(24.969 \pm 0.007)\,\mathrm{ns}$ almost fills the complete acceptance window of one clock period. The last information from this measurement is that the rising time of the efficiency is small, it rises in below $1\,\mathrm{ns}$ to almost its maximal value.
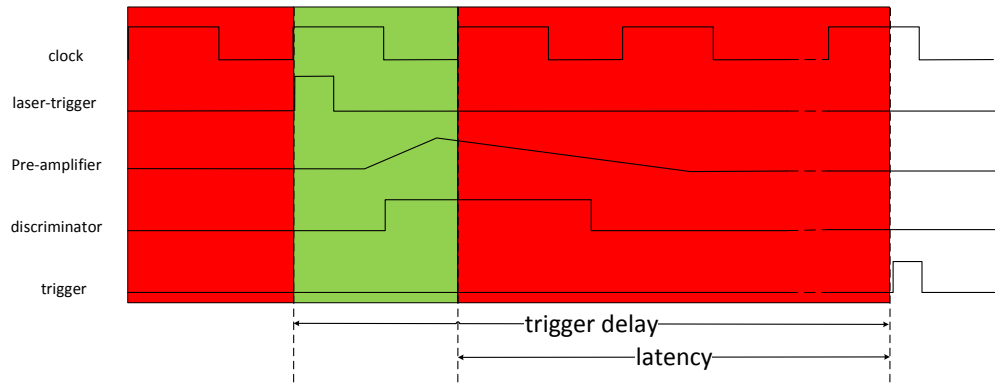
Figure 5.2.: Behaviour of the system for correct timing. The green zone indicates the set acceptance window whereas the red ones indicate zones where a hit is not accepted as a result of wrong timing.
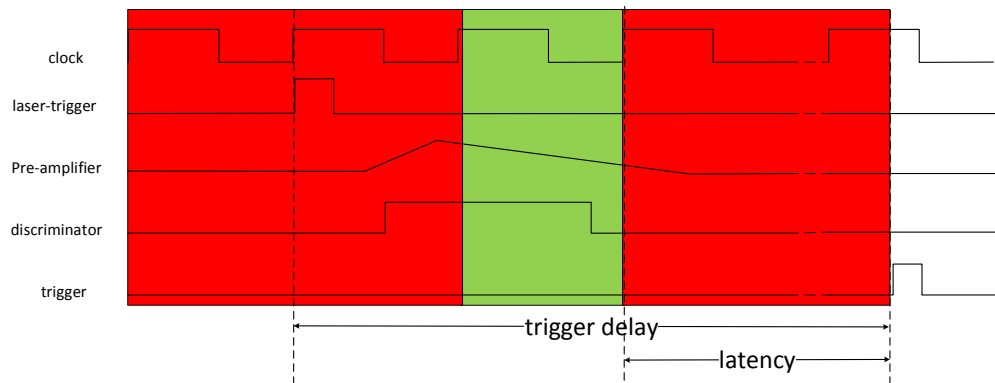
Figure 5.3.: Behaviour of the system for incorrect timing. The hit (rising edge on the discriminator output) occurs in the non-acceptance region (red) and the read-out trigger will not be responded with a hit.

Furthermore, the dependence of the in-time efficiency on the injected charge was investigated (timewalk). The probability of detection, the signal to noise ratio and the charge collection efficiency decrease for smaller charges and the in-time efficiency also decreases. This decreasing behaviour is design-dependent and another approach to compare different module concepts.
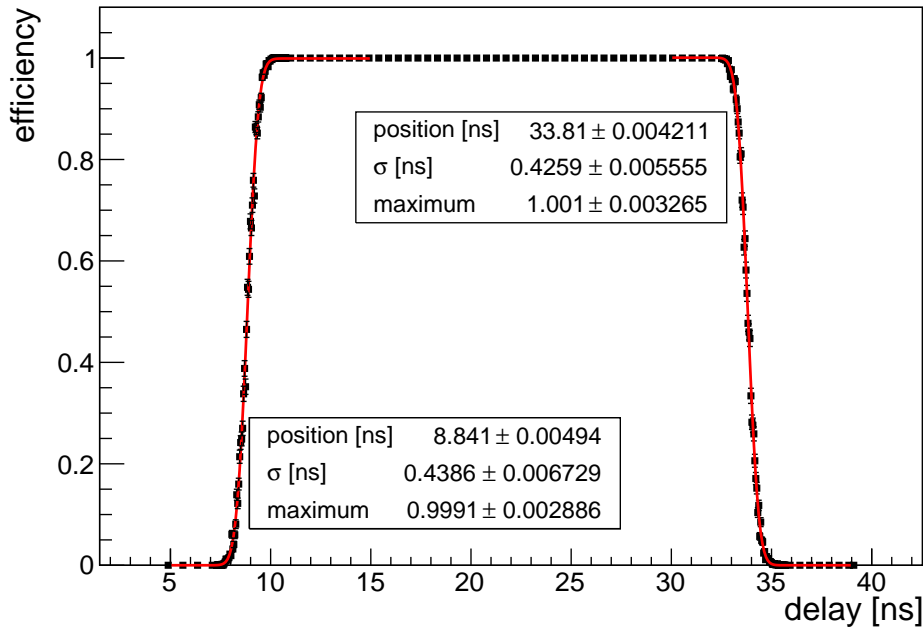
Figure 5.4.: In-time efficiency measurement of module A. The FWHM is about 24.97 ns
and covers nearly the complete acceptance window of 25 ns.

5.2. Timewalk

The timewalk was measured for module A (compare Section 4.4) pixel 35/167, the result
is shown in Figure 5.5. Both measurement techniques were used in order to compare
them (see Section 3.4). Figure 5.5 (a) shows a measurement using the laser setup and
the photodiode calibration for charge information. Figure 5.5 (b) shows the internal mea-
surement with charge information using the VCAL-to-charge calibration and the laser
measurement with charge information using the ToT calibration.

Unfortunately, the transformation of pin voltage to injected charge for the laser mea-
surement (from Section 4.5.2) did not work. The smallest injected charges begin at
around 800 e (compare Figure 5.5 (a)) which can not be true as the module is tuned to a
threshold of 3000 e. This mismatch may be a result of different reflectivity of module A
and C. Fortunately, it is also possible to use the ToT information of the laser measure-
ments as measure for the injected charge. In theory, the intensity calibration using the
photodiode is more accurate compared to the ToT calibration as a result of the limited
resolution of the ToT information (0-15, 4 bit). Nevertheless, some unknown systematic
problems makes the photodiode calibration unusable. Therefore, the ToT calibration and

the VCAL-to-charge calibration are used to obtain the charge information for Figure 5.5 (b).

The absolute y-values in Figure 5.5 (b) are measured relative to an arbitrary clock pulse. Therefore, the plateau region in the high charge regime of the internal method was fitted to the plateau region of the laser measurement.

It can be seen that both methods exhibit a plateau for high injected charge values since the rising slope of the preamplifier saturates (compare Figure 3.5). That means, at some point, an increased injected charge does not lead to a further increased slope of the preamplifier. Consequently, the delay is not further reduced and the timewalk saturates as it can be seen in Figure 5.5 (b). As the slope of the preamplifier output starts to decrease with decreasing charge in the middle regime (8000-15 000 e) both methods show the expected rising behaviour. Moreover, they show very similar results in this region. In the low charge region, they separate slightly from each other which is explained by the bad charge resolution for the laser measurement.

The in-time threshold is the minimal amount of injected charge which is needed to limit the timewalk below 20 ns above the plateau. This timespan is chosen in order to keep hits within the 25 ns acceptance window given by the LHC beam clock with an additional 5 ns safety margin. In this case, the plateau region is located at a delay of about 35 ns. Therefore, the in-time threshold is the charge which is needed to be injected in order to be observed at a delay of 35 ns. Both measurements are as close to the threshold as possible which is why the in-time threshold is very close to the threshold being (2910 ± 40) e.
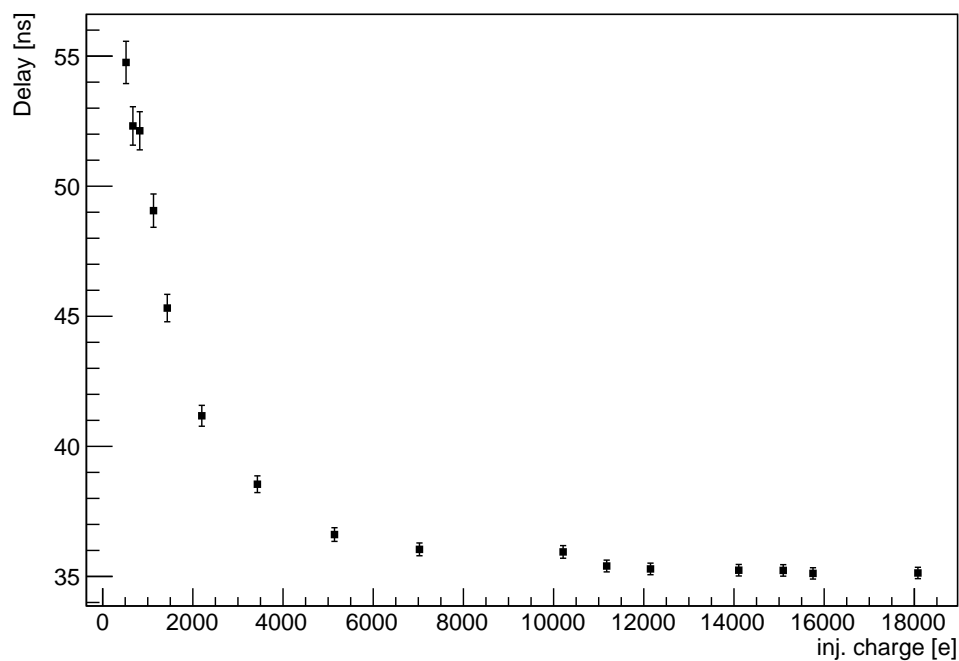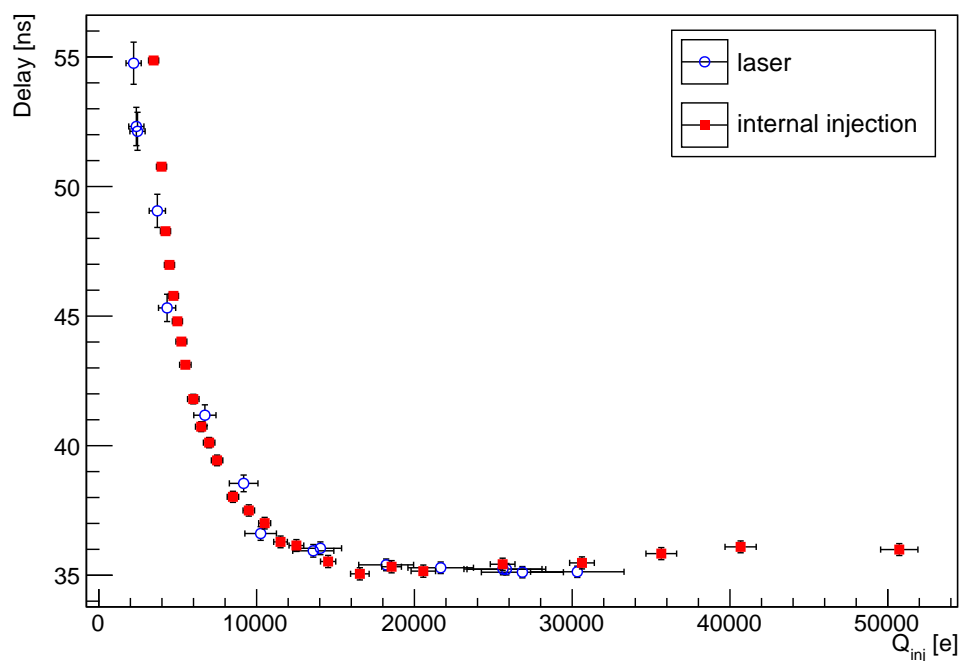
(a) laser setup

(b) internal injection

Figure 5.5.: Timewalk of module A: (a) measured with the laser setup and pin-diode for charge calibration and (b) the internal injection and laser measurement using VCAL-to-charge and ToT calibration.

5.3. Tuning of IBL using DisVbn

In IBL, two front-ends share one connection to read-out chain (TTC link). Manufacturing margins cause a different timing behaviour between different front-ends. Timing differences between TTC links are compensated via another delay-parameter in the back of crate card (BOC, component of the read-out chain) to 100 ps precision. Nevertheless, the difference between two front-ends sharing the same TTC link needs to be compensated. As the delay of a front-end was found to be rather sensitive to the *DisVbn* parameter, it is a possibility to tune the timing behaviour via the *DisVbn* value of each module. Therefore, the timing behaviour of module B was characterised and two different measurement principles are compared in this thesis.

Thermal and power restrictions prohibit the use of extremely high values of *DisVbn* in IBL. Consequently, a value of 40 is chosen for the faster front-end whereas the other front-end uses a higher *DisVbn* value (determined using the internal method) in order to match the timing behaviour of the first front-end.

In principle, the variations in the timing behaviour either result from the charge injection itself or the hit recording apparatus. While the latter effect needs to be determined as precisely as possible, the first issue must be excluded. In order to verify the internal injection method, the laser setup is used to remeasure the behaviour. For the laser setup, the determined timewalk just results from the hit recording chain.

- **Laser measurement:**
  The laser setup is used as described in Section 4.6. *Strobe_fine_delay* is varied within a certain range which is chosen that it contains the rising edge of the occupancy. A *Delay_fit*[1] is used in order to determine the position of the rising edge. Then, a loop over *DisVbn* values in the area of interest from 40 to 80 results in the wanted behaviour of the delay against *DisVbn*. In order to prevent any additional effects caused by timewalk, a reasonably large charge ($\gg 20000\,\mathrm{e}$) is injected resulting in a mean ToT value of 8.

- **Internal measurement:**
  The internal measurement uses the integrated injection mechanism of each front-end (compare Section 3.3) in combination with the also integrated delay mechanism (parameter *Strobe_Delay*). Thus, the internal injection is delayed and a turn-on curve is observed (T_0_Scan). The position of the rising edge of the occupancy is

---

[1]iterative determination of the 50% point

also obtained via a *Delay_fit*. Consequently, both measurement principals are very similar.

a	39.09 ± 0.231
b	−1260 ± 12.98
a	39.39 ± 0.2464
b	−1279 ± 13.85
a	41.7 ± 0.2254
b	−1295 ± 12.67

Chip 0 col 7 row 9
Chip 0 col 7 row 12
Chip 0 col 79 row 6
Chip 1 col 78 row 35
Chip 1 col 78 row 38
Chip 1 col 15 row 6

a	44.59 ± 0.2447
b	−1678 ± 13.76
a	43.13 ± 0.2411
b	−1639 ± 13.55
a	45.1 ± 0.1749
b	−1676 ± 9.83
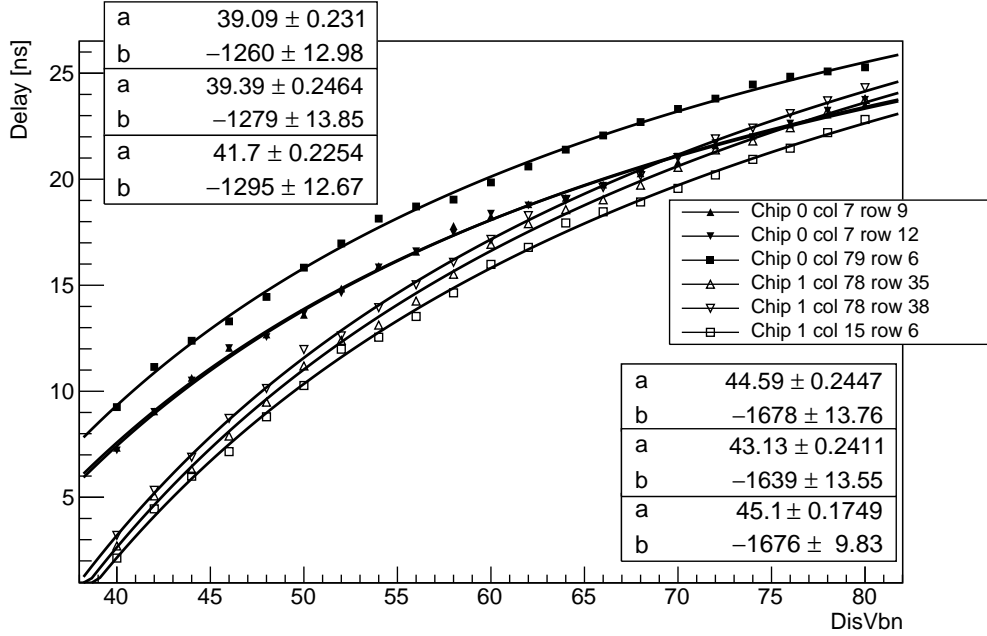
Figure 5.6.: Behaviour of the delay of the IBL module against *DisVbn* using the laser setup for different pixels on both front-ends. A fit-function of the type $f(x) = a + \frac{b}{x}$ was used. Included statistical errors are not visible, additional systematic errors are not shown.

Figure 5.6 shows the timing measurements of different pixels on both front-ends of the IBL module using the laser injection method. A fit of the type $f(x) = a + \frac{b}{x}$, as indicated by Section 3.5, is applied. The shown errors are statistical errors whereas the additional systematic errors are not shown because they can not be assessed. The individual pixels are chosen from different regions of the front-end in order to compare structural differences. Spatial differences are expected as a result of manufacturing margins between different pixels and front-ends. Also, the power distribution is known to be not fully homogeneously which causes further differences between distant pixels. Considering this expected inequality between different pixels and front-ends the results are consistent.

Figure 5.7 shows a comparison of the laser and internal injection method for both front-ends. Figure 5.7 (a) shows significant differences for front-end 0. In contrast, Figure 5.7 (b) shows good agreement between laser and internal injection on front-end 1. Both figures are representative, four pixels were measured on both front-ends and all results

(a) 0/79/6

(b) 1/78/38
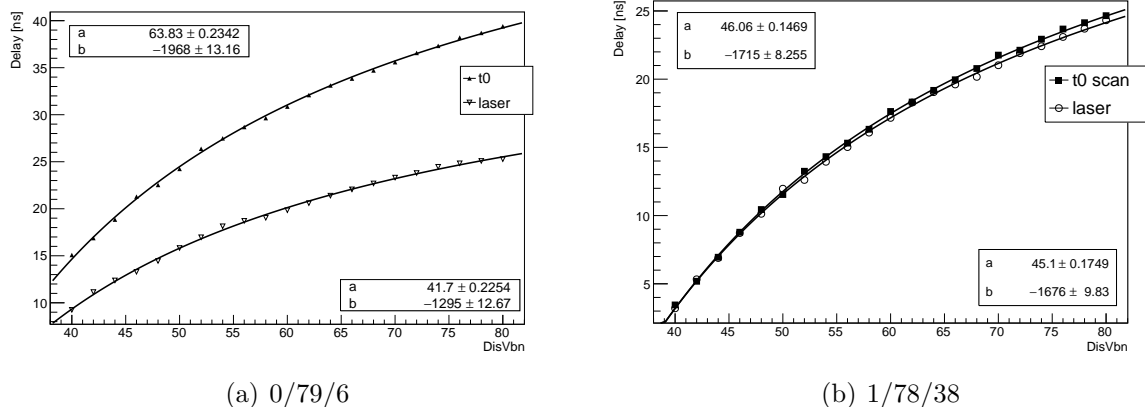
Figure 5.7.: Behaviour of the delay of the IBL module (module B) against *DisVbn* using the internal injection mechanism for (a) pixel 79/6 on front-end 0 and (b) pixel 78/38 on front-end 1. A fit-function of the type $f(x) = a + \frac{b}{x}$ was used. Included statistical errors are not visible, additional systematic errors are not shown.

look similar to the shown plots.

Since there is a good agreement between laser and internal injection for front-end 1, the calibration of the internal delay mechanism is suspicious for front-end 0. For this calibration the delay (in DAC units) is measured for two different *Trigger_Delay* values which results in a known time difference (in time units) of one clock-cycle. However, the calibration is only possible if a measurement of the delay is achieved for two different *Trigger_Delay* values. As a further investigation shows, this requirement is not fulfilled for front-end 0 because the accessible time-range of the *Strobe_Delay* is not sufficient. Nevertheless, the calibration is necessary for the internal injection method. The remedy in this case is the *PlsrdacRamp* parameter which determines the step size of the internal delay mechanism. A decreased *PlsrdacRamp* parameter ($213 \rightarrow 150$) provides valid delay measurements for both front-ends for two *Trigger_Delay* values.

Figure 5.8 shows the results for the new calibrated internal delay mechanism. Now the results for front-end 0 look consistent for the two methods. Again, various pixels are measured and the shown plot is a representative example. The remaining difference between both methods most likely is still caused by the delay mechanism calibration which is now valid but still not very precise. Fluctuations between different pixels on the same front-end are in the order of $5 - 15\%$ whereas there is just one calibration parameter for the whole front-end. Consequently, per-pixel evaluations have to be analysed with this

additional systematic error which is not included in the plot.
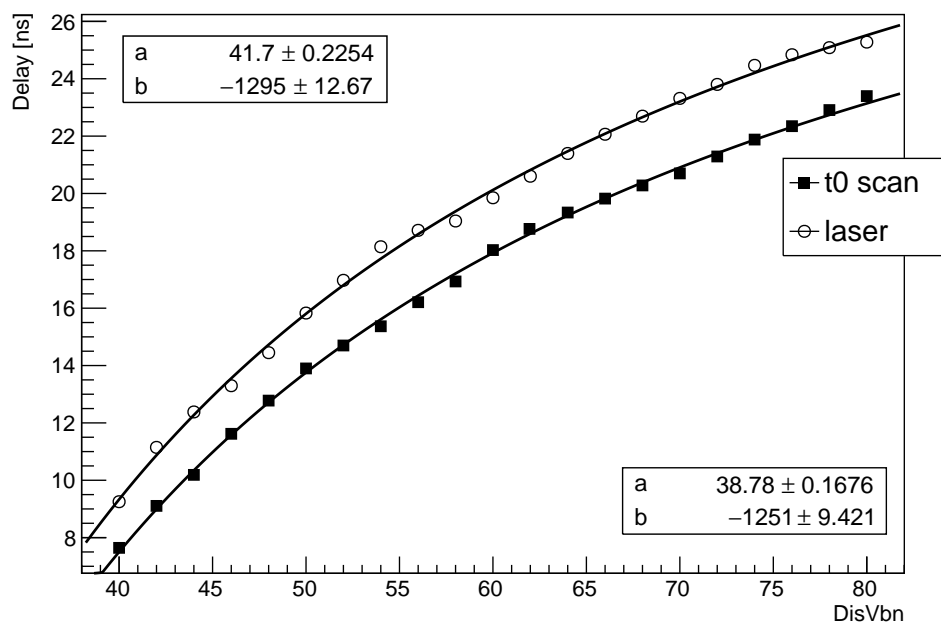
Figure 5.8.: Behaviour of the delay of the IBL module against *DisVbn* using the internal injection mechanism and the new calibration for pixel 79/6 on front-end 0. A fit-function of the type $f(x) = a + \frac{b}{x}$ was used. Included statistical errors are not visible, additional systematic errors are not shown.

6. Spatially resolved hit efficiency

Ideally, the spatially resolved hit efficiency is uniform over the whole area of the pixel. Consequently, the pixel recognises a hit regardless if it occurs in the central region of the pixel or at the edge of it. The spatially resolved hit efficiency is determined for new sensor concepts which is possible using the laser setup. Therefore, the laser is sampled in small steps (here: 2 µm) over the surface of the sensor, injecting charge several times (here: 1000) at each position. The result is a hit efficiency map regardless of the size of the individual hit as well as a mean ToT value for each point (ToT map) of all involved pixels. Moreover, there is the possibility to analyse exclusive plots of individual pixel with a veto if other, adjoining pixel see the hit as well. For all of these plots a new program was developed during this thesis in order to analyse the produced raw data files.

6.1. Setup

The setup is analogous to the composition described in Section 4.6 (compare Figure 4.13). The laser intensity is monitored with the photodiode (compare Section 4.5.2). Even though variations of the laser intensity over time are expected from previous theses [55], no significant change was found. As there are several interruptions during a scan caused by read-out breaks initiated by STControl, the thermal conditions are much more stable compared to the continuous operation mode of previous measurements (compare Section 4). Stable intensity conditions are very important for spatially resolved hit efficiency measurements because they take up to 20 hours, depending on the scanned area and the resolution.

6.2. Hit efficiency maps

Hit efficiency maps are plotted for module A. The scanned area is always $256{\times}256\,\text{µm}^2$ using a step-size of 2 µm resulting in 15876 scan points. At every position, 1000 laser-pulses are fired onto the sensor. The efficiency for every position is then calculated using the total number of hits divided by 1000. Thereby, multiple hits resulting from one injection

are identified using their timestamp.

The exact position on the module is chosen so that the edge of the metallization is visible in the top part of the scanned area. Four different charges are chosen in order to visualise the effect of different charges especially in comparison of charges close to the threshold to large charges. Figure 6.1 shows the efficiency maps for all measured laser intensities.

(a) low charge

(b) medium (-) charge

(c) medium (+) charge

(d) high charge
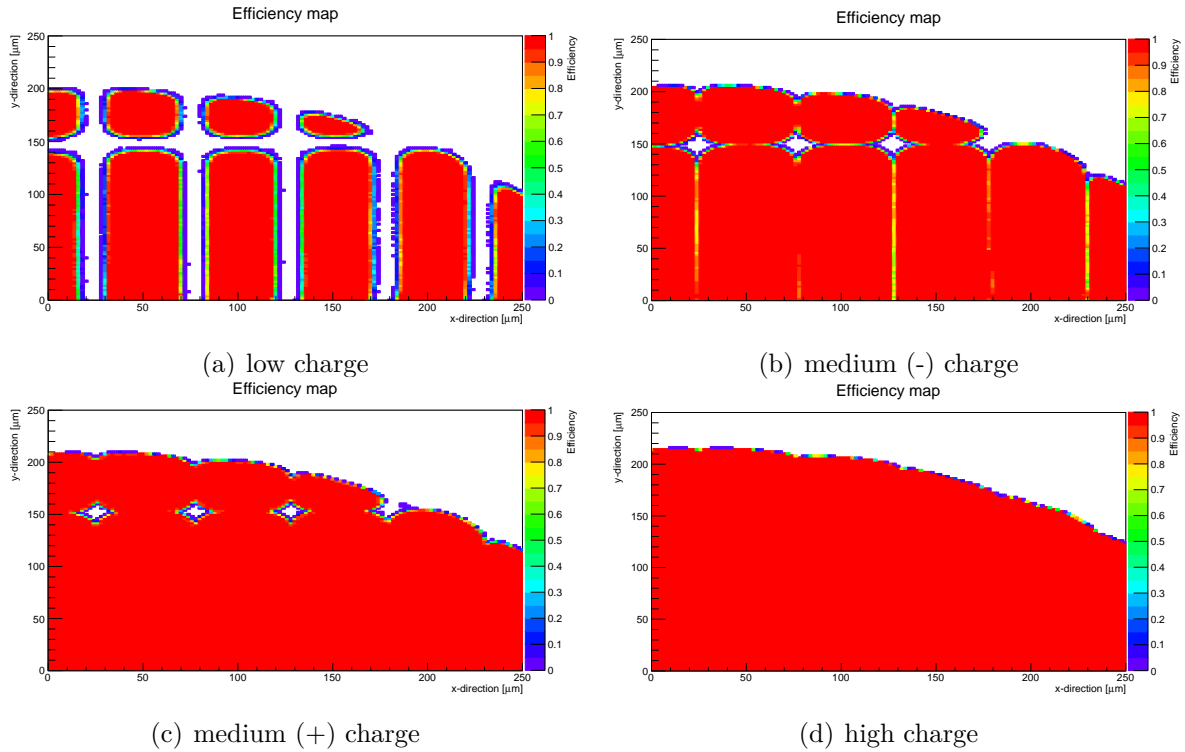
Figure 6.1.: Hit efficiency maps of module A for four different charges. The individual injected charge is calculated from the photodiode voltage and the ToT calibration as mentioned in the text.

A qualitative point of view shows that measurement (a) is done close to the threshold as there are still inefficient areas between the central regions of the pixels. Those inefficient regions are a result of charge sharing. If the charge is shared about equally between two pixels, none of their discriminators will be exceeded. Consequently, the injected charge is smaller than two times the threshold. Nevertheless, the central regions are already 100% efficient. As the injected charge is increased from (a) to (b) and (c), the inefficient areas on the sides of the pixels become effective, whereas the area between four pixels is still ineffective. Here, the charge is shared between four pixels and thus has to be at least four times the threshold in order to induce a hit. This is achieved by a further increased charge (d). It leads to a complete coverage of the accessible region with a homogeneous efficiency of 1. The injected charge is now at least four times the threshold.

The injected charges are one-time calculated using the photodiode and one-time using the ToT calibration (Table 6.1). The charges according to the photodiode are calculated using the pin diode voltage which was noted for each measurement. For the ToT related charges, the mean ToT value in the central region of the calibrated pixel was determined. The charges as indicated by the photodiode seem systematically to low. As the front-end

	$Q_{\mathrm{photodiode}}$ [e]	Q_{ToT} [e]
low charge	820 ± 860	6700 ± 500
medium (-) charge	2050 ± 870	9300 ± 700
medium (+) charge	2650 ± 880	9300 ± 700
high charge	8000 ± 1100	$20\,000 \pm 3500$

Table 6.1.: Injected charges for all measurements calculated using the photodiode and ToT calibration, respectively.

is tuned to a threshold of around $3000\,\mathrm{e}$, no hits should be observable below this value. This systematic error may be because of a different reflectivity of module A and C, as mentioned before.

Exclusive efficiency means that every coincidental hit vetoed any hits for this trigger. Consequently, the efficiency is calculated as the number of separate hits in the pixel of interest divided by 1000. Thereby, hits are counted to be separately if no other hit is recorded within 4 clock cycles. The corresponding results are shown in Figure 6.2. They show that the efficient area first grows with increasing charge ((a)→(c)) before it decreases again (d) as a result of charge sharing between adjacent pixels caused by the large injected charge. The separated points around the efficient area in Figure (d) are caused by large timewalk (>4 clock cycles). That makes them look like an individual hit even though there was a coincident hit.

6.3. ToT maps

Besides the information of whether a hit is observed by a pixel or not, the mean ToT value is a measure on how effective the charge collection works in the sensor. The low injected charge measurement in Figure 6.3 (a) again shows ineffective areas between the pixels. The ToT is maximal in the center of each pixel and falls to the edges. This is due to charge sharing with adjacent pixels whereby the shared charge does not exceed the threshold of the adjoining pixel. With increasing charge ((b) and (c)), the gaps between

(a) low charge

(b) medium (-) charge

(c) medium (+) charge

(d) high charge
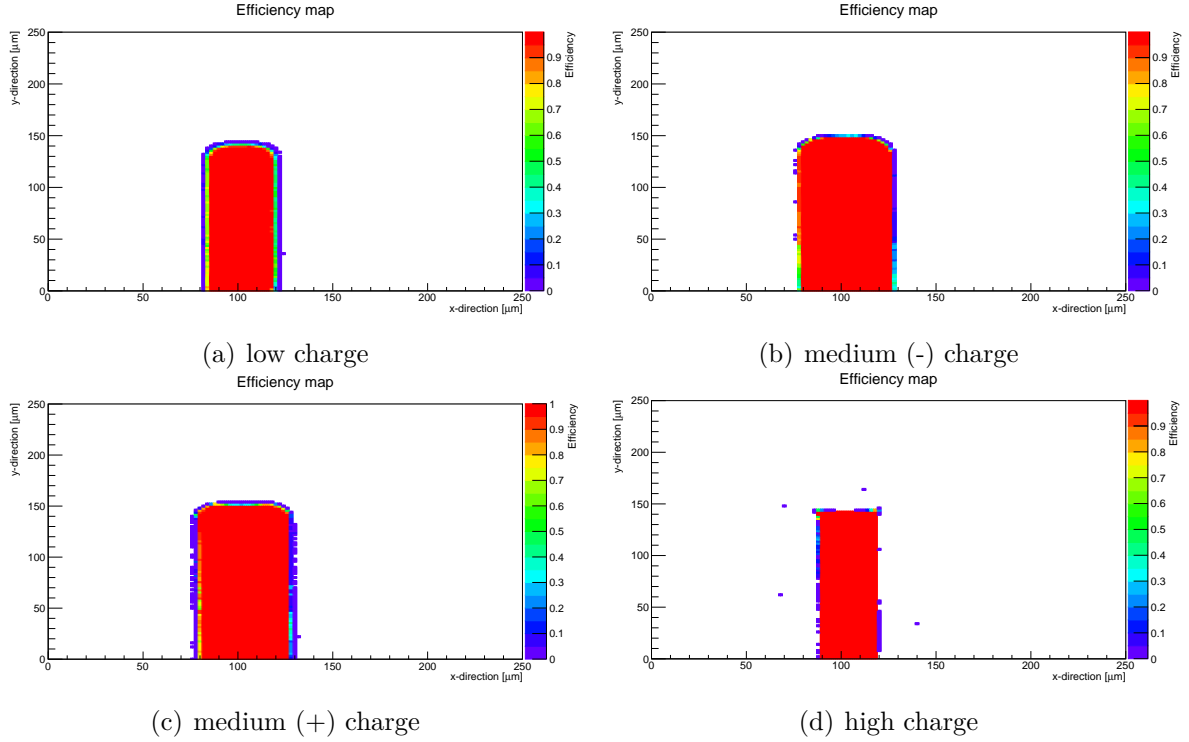
Figure 6.2.: Exclusive hit efficiency maps of module A for four different charges. Exclusive efficiency means that every coincidental hit vetoed a hit for the shown pixel. The individual injected charge is calculated from the photodiode voltage and the ToT calibration as mentioned in the text.

the pixels become closed and the maximal ToT rises. The maximal ToT is still in the central region of each pixel and it decreases to the edges. This is again due to charge sharing whereby part of the charge is collected by adjacent pixels and not measured since the threshold is not exceeded. The areas between four pixels are still ineffective. Here, the charge is shared between four pixels and thus can not exceed the threshold of all four pixels. That changes with a further increased charge (d), where the full accessible region is now covered. The maximal ToT is now located between adjacent pixels, especially in the area between four pixels. The large charge spreads up on the way through the sensor to the read-out and is shared between all four pixels. As the ToT-to-charge calibration has a second order polynomial shape, several small charges in different pixels add up to a higher overall ToT compared to one large charge in one pixel.

In order to quantify the charge-sharing region, the projection onto the x-axis is done for all charges (Figure 6.4 shows the plot for the high injected charge, Figure A.1 in the appendix shows all other plots). The region from 0 to 100 µm is chosen for the projection

(a) low charge

(b) medium (-) charge

(c) medium (+) charge

(d) high charge
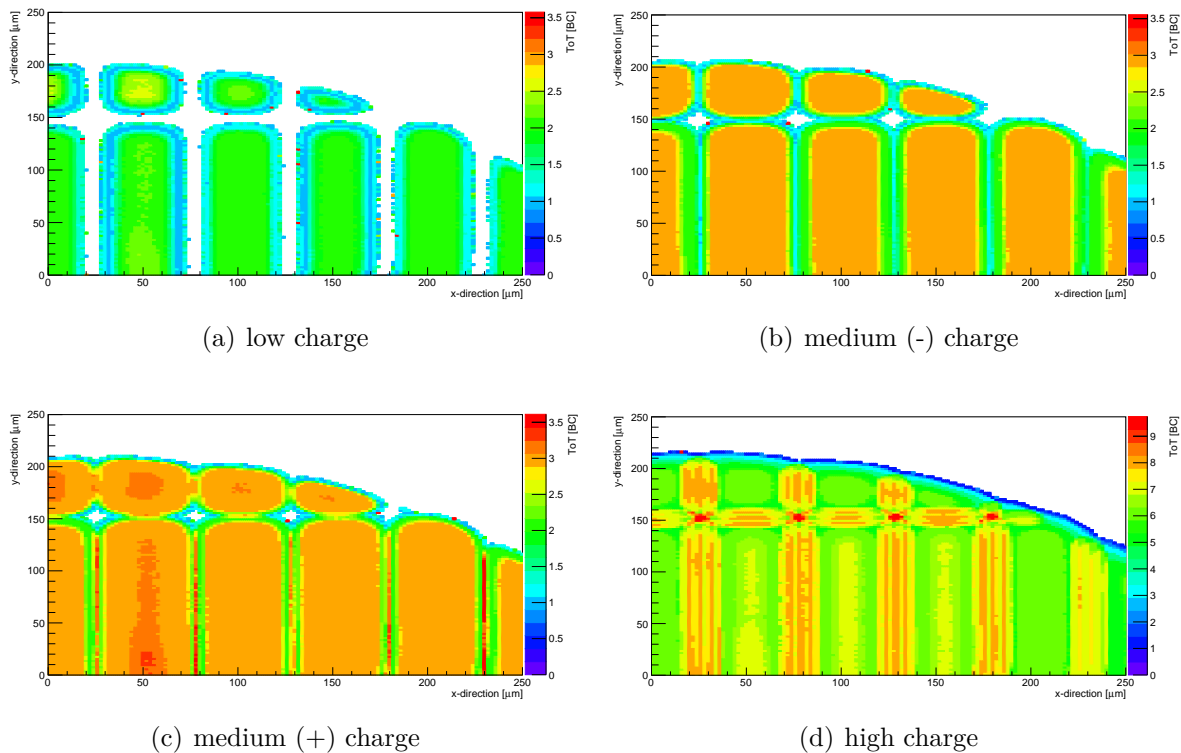
Figure 6.3.: ToT maps of module A for four different charges. The individual injected charge is calculated from the photodiode voltage and the ToT calibration as mentioned in the text.

in order to avoid boundary effects from the metallization edge. The width of the central part of the pixel as well as the charge-sharing region between adjacent pixels is determined by the projection. For the three smaller charges, charge-sharing is not distinguished from efficiency losses because the shared charge can not exceed both thresholds and is therefore not registered. Consequently, the sharing width values for those charges are not meaningful. In contrast, however, the value for the central width for the largest charge is not applicable because it is overlapped by the charge sharing zone. The mean widths of the charge-sharing/central regions are given in Table 6.2. The inapplicable results are marked in the table using braces. All values are measured using a fit of the function

$$f(x) = a + 0.5 \cdot b \cdot \left(\text{erf}(\frac{x - c_1}{d}) - \text{erf}(\frac{x - c_2}{d}) \right) \tag{6.1}$$

61

where erf() is the error function and c_1 and c_2 determine the width (σ) of the charge sharing zone

$$\sigma = c_2 - c_1. \tag{6.2}$$

This function is chosen because it represents a two-sided turn-on curve. The fit region is adapted by hand to be [edge$_1$-10,edge$_2$+10]µm with edge positions determined by eye in order to improve the fit.

Charge [e]	sharing width [µm]	central width [µm]
low charge	(23.3 ± 1.5)	27.0 ± 3.4
medium (-) charge	(18.3 ± 1.9)	34.4 ± 3.7
medium (+) charge	(14.0 ± 1.4)	38.0 ± 2.8
high charge	21.5 ± 1.3	(30.1 ± 0.1)

Table 6.2.: Central and sharing width of the measured pixels as a result of the x-projection. Values in braces indicate inapplicable results because charge sharing is indistinguishable from efficiency losses for the three smaller charges and the charge sharing zone overlaps the plateau for the largest charge.
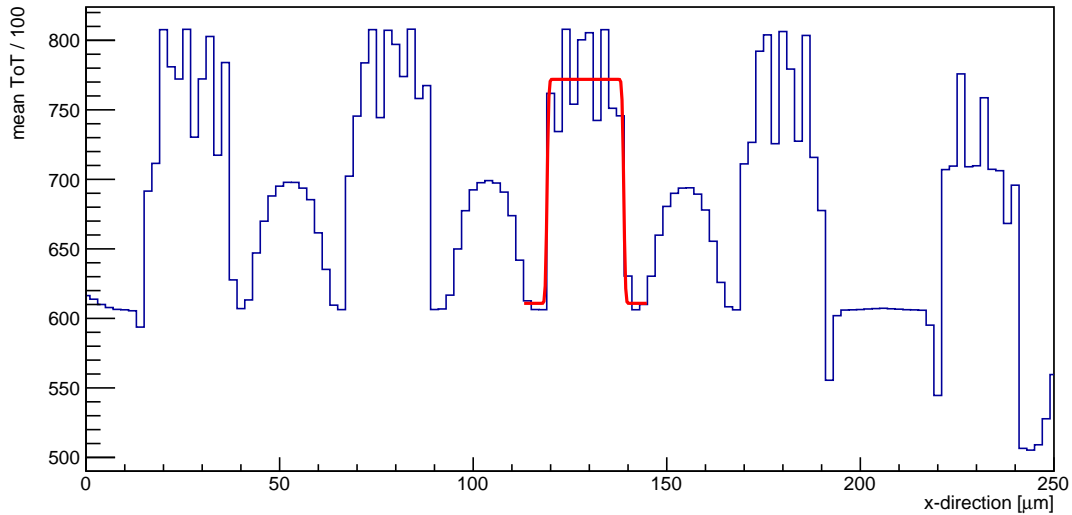
Figure 6.4.: Projection on the x-axis from the ToT map for high charge injection with exemplary and representative fit of one charge sharing zone.

The observed charge sharing widths are compared to the expected diffusion of the de-

posited charge. The radial diffusion width [47] is calculated by

$$\sigma(r) = \sqrt{6Dt} \tag{6.3}$$

to be about $8.1\,\mu\mathrm{m}$ in each direction for a drift velocity of $v_\mathrm{D} = 1.0 \times 10^7\,\mathrm{cm\,s^{-1}}$, a diffusivity of $D \approx 36\,\mathrm{cm^2\,s^{-1}}$ [60] and a drift length of $300\,\mu\mathrm{m}$. Assuming the charge to be initially deposited within a $5\,\mu\mathrm{m}$ diameter, the charge cloud has a diameter of about $21.2\,\mu\mathrm{m}$ after drifting through the sensor. This means that charge carriers reach the read-out electrode of a pixel even if the charge is deposited up to $21.2\,\mu\mathrm{m}$ away. This calculation is confirmed by the measured charge sharing zone of $(21.5 \pm 1.3)\,\mu\mathrm{m}$.

Finally, the pixel pitch is calculated by summing up the central and sharing widths. The average over all injected charges is $(51.6 \pm 6.4)\,\mu\mathrm{m}$ which confirms the expected pitch of $50\,\mu\mathrm{m}$.

7. Conclusion and Outlook

In order to cope with the challenges of a future HL-LHC, different sensor concepts are under investigation for an operation in the ATLAS Inner Tracker. The motivation for this thesis is the development of methods to investigate time-resolved and spatial-resolved hit efficiencies. All those methods use the probestation with laser setup for precise charge injection. Therefore, the probestation is set up using the USBPix system for read-out and timing and STcontrol as software to control the setup. Different control-measurements are performed and the spot size is determined to be sufficiently small. Next, the laser intensity is calibrated using a photodiode in order to have an external monitoring of the injected charge.

The first developed method for future sensor testing are time-resolved hit efficiency measurements. The in-time efficiency is determined and by modifying the injected charge, the timewalk is identified. Both depend on the charge collection process in the sensor, which is why they are expressive quantities when classifying new sensor concepts and prototypes. Here, the most important improvement over former measurements using the internal injection circuits is that the laser-injection and delay mechanism are completely independent of the module. Consequently, effects due to the hit-detection and not caused by the hit-production are observed. This circumstance was the key for the verification of the IBL timing tuning, where the behaviour of the *DisVbn* parameter was investigated. This is a contribution to the soon published IBL production and integration paper [40].

Besides the time-resolved hit efficiency measurements, the spatially resolved hit efficiency is measured with the probestation setup. The results consist of efficiency maps showing whether any hit is recorded or not. In addition, ToT coded maps are available where the mean ToT value for each position is calculated. From this map, an x-projection is used to determine the charge sharing region and the pixel pitch. For module A, the charge sharing region for large charges is determined to be $(21.5 \pm 1.3)\,\mu\text{m}$ and thus confirming theoretical expectations based on charge diffusion. Also, the pixel pitch is $(51.6 \pm 6.4)\,\mu\text{m}$, confirming the expected size of the pixel of $50\,\mu\text{m}$.

7. Conclusion and Outlook

While the probestation and laser setup can be used for all kind of sensor concepts, a few requirements have to be considered for future tests. The red laser can just be used for sensors without a top layer metallization or at least with holes in it. The IR laser was not tested yet but it might be an opportunity to inject charge through the metallization. Although, new methods for the calibration of intensity and spot-size will be required.

The laser assisted probestation turns out to be a very good opportunity for future module prototype tests. Precise timing and spatially resolved efficiency measurements can be performed. Particularly the spatially resolved efficiency maps can give a good overview when testing new modules. Thereby, the external control of charge injection and timing has important advantages against the front-end internal opponents. All observed effects are just by reason of hit recognition and do not depend on any integrated and front-end specific injection mechanisms.

Although the conceptionally benefits worked out very well, specific parts have to be modified. Especially the laser intensity monitoring using the photodiode did not work out. Possible reasons are thermal instabilities of the photodiode itself, thermal instabilities of the beam guidance system or differences in the reflectivity of the used modules. Moreover, the spot size of the laser was determined for one intensity. Despite the structure size for the different injected charges of the efficiency- and ToT-maps are looking rather similar, the intensity tends to have an influence on the spot-size. Therefore, the spot size should be evaluated for different intensities.

A. Appendix
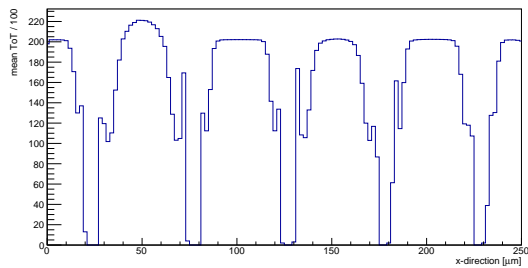
(a) low charge
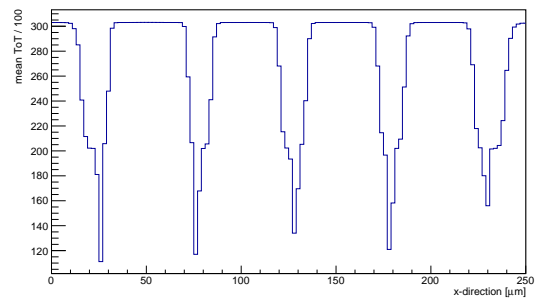
(b) medium (-) charge
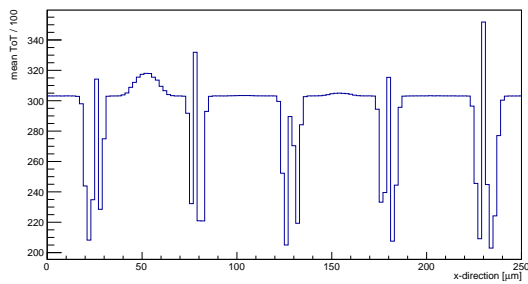
(c) medium (+) charge
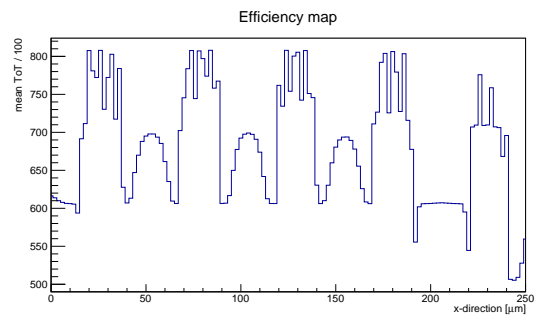
(d) high charge

Figure A.1.: Projection on the x-axis from the ToT map for all charges.

(a) *ToT_verify* scan

(b) *ToT_verify* scan

(c) *Threshold_Scan*
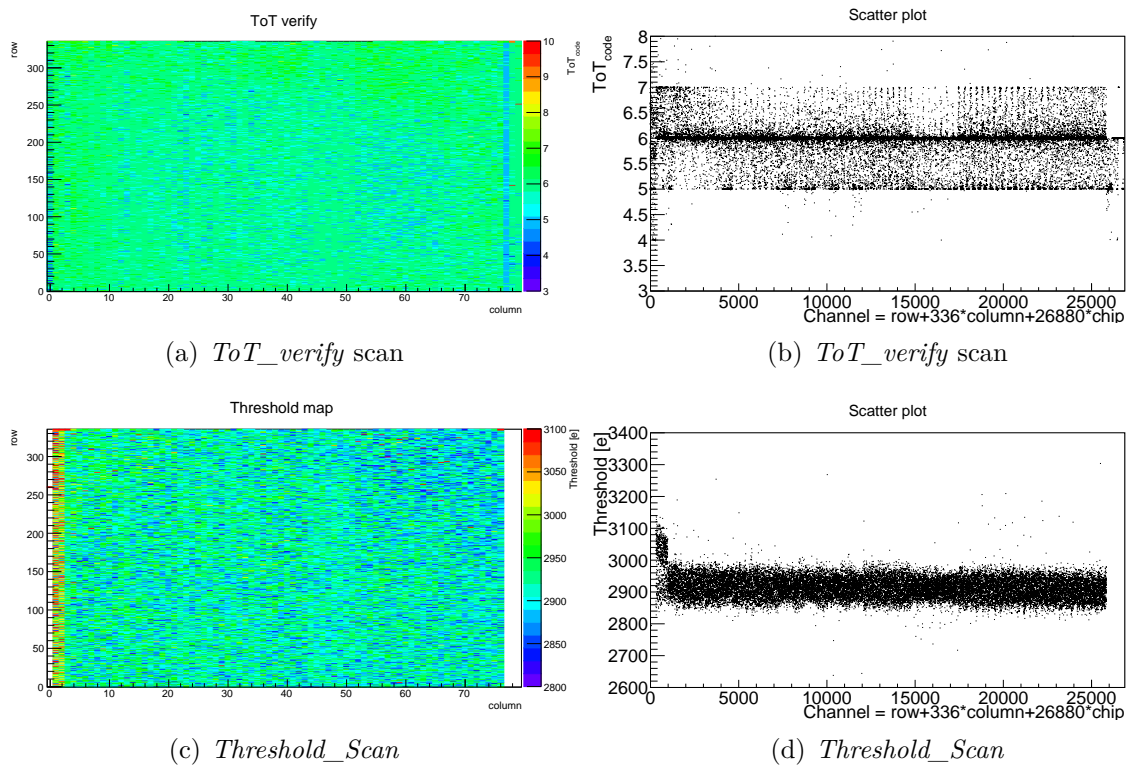
(d) *Threshold_Scan*

Figure A.2.: Characterisation of module A. The result of the *ToT_verify* scan is a ToT value of 5.9 ± 0.4 for an injected charge of 20000 electrons. The result of the *Threshold_Scan* is a threshold of $(2910 \pm 40)\,\text{e}$.

(a) *ToT_verify* scan

(b) *ToT_verify* scan

(c) *Threshold_Scan*
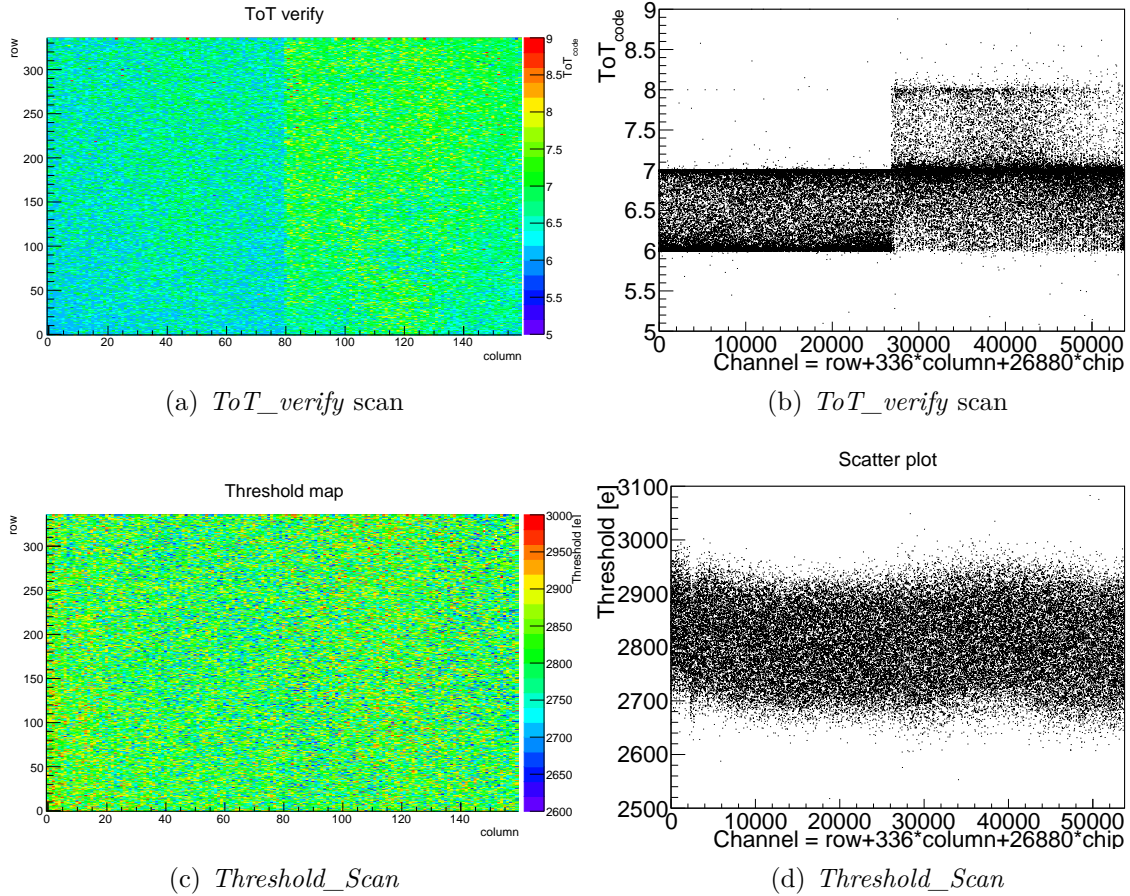
(d) *Threshold_Scan*

Figure A.3.: Characterisation of module B. The result of the *ToT_verify* scan is a ToT value of $(6.7 \pm 0.4)\,$e for an injected charge of 20000 electrons. The result of the *Threshold_Scan* is a threshold of $(2827 \pm 97)\,$e.

(a) *ToT_verify* scan

(b) *ToT_verify* scan

(c) *Threshold_Scan*
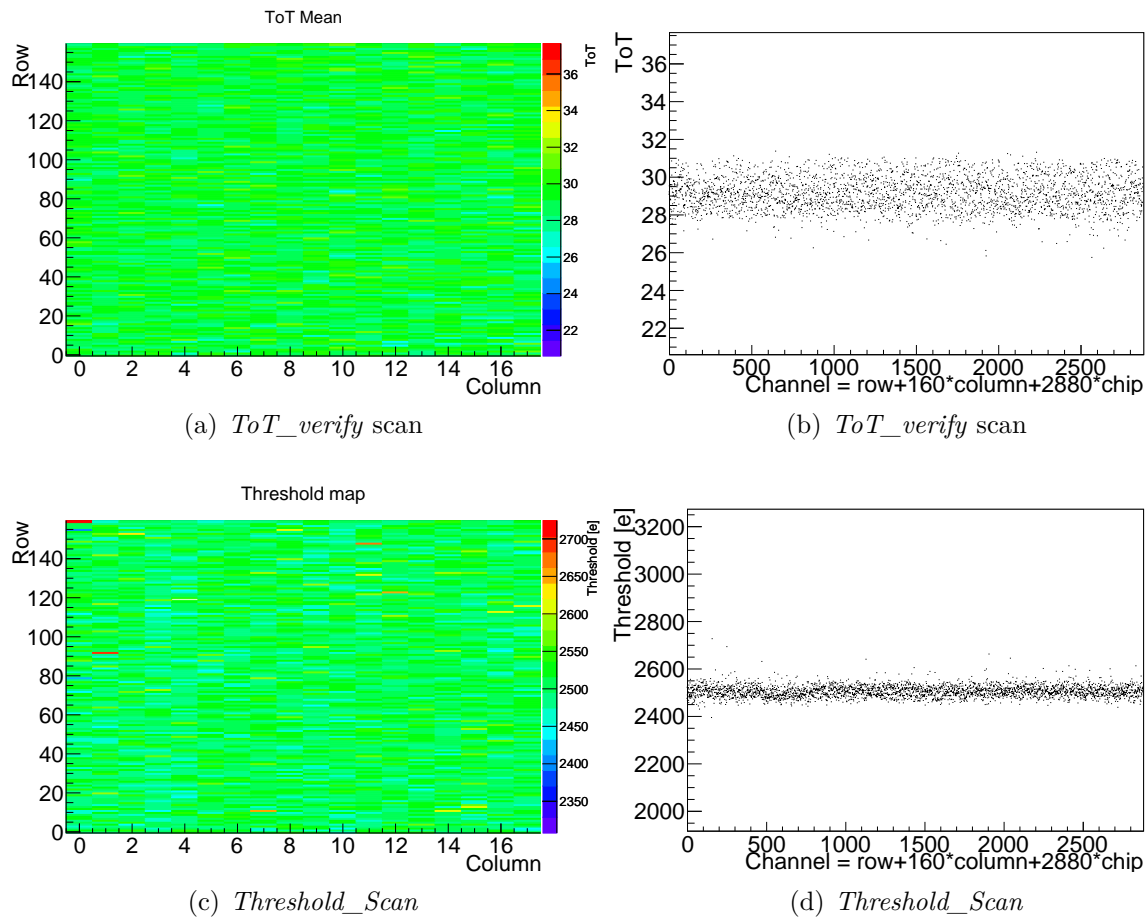
(d) *Threshold_Scan*

Figure A.4.: Characterisation of module C. The result of the *ToT_verify* scan is a ToT value of 29.1 ± 0.9 for an injected charge of 15000 electrons. The result of the *Threshold_Scan* is a threshold of $(2505 \pm 25)\,\mathrm{e}$.

Bibliography

[1] D. Griffiths, *Introduction to Elementary Particles*, Wiley-VCH (2008)

[2] J. J. Thomson, *XL. Cathode Rays*, Philosophical Magazine Series 5 **44(269)**, 293 (1897)

[3] M. Breidenbach, et al., *Observed Behavior of Highly Inelastic Electron-Proton Scattering*, Phys. Rev. Lett. **23**, 935 (1969)

[4] E. D. Bloom, et al., *High-Energy Inelastic $e - p$ Scattering at 6° and 10°*, Phys. Rev. Lett. **23**, 930 (1969)

[5] S. H. Neddermeyer, C. D. Anderson, *Note on the Nature of Cosmic-Ray Particles*, Phys. Rev. **51**, 884 (1937)

[6] E. D. Courant, M. S. Livingston, H. S. Snyder, *The Strong-Focusing Synchroton - A New High Energy Accelerator*, Phys. Rev. **88**, 1190 (1952)

[7] G. Danby, et al., *Observation of High-Energy Neutrino Reactions and the Existence of Two Kinds of Neutrinos*, Phys. Rev. Lett. **9**, 36 (1962)

[8] S. L. Glashow, J. Iliopoulos, L. Maiani, *Weak Interactions with Lepton-Hadron Symmetry*, Phys. Rev. D **2**, 1285 (1970)

[9] B. Richter, *From the psi to charm: The experiments of 1975 and 1976*, Rev. Mod. Phys. **49**, 251 (1977)

[10] S. C. C. Ting, *The discovery of the J particle: A personal recollection*, Rev. Mod. Phys. **49**, 235 (1977)

[11] J. W. Cronin, V. L. Fitch, R. Turlay, *Evidence for the 2π Decay of the K_2^0 Meson*, Phys. Rev. Lett. **13**, 138 (1964)

[12] M. Kobayashi, T. Maskawa, *CP-Violation in the Renormalizable Theory of Weak Interaction*, Prog. Theor. Phys. **49(2)**, 652 (1973)

Bibliography

[13] L. M. Lederman, *Lepton Pair Production in Hadronic Collisions*, NATO Sci.Ser.B **39**, 1 (1979)

[14] W. R. Innes, et al., *Observation of structure in the Υ region*, Phys.Rev.Lett. **39**, 1240 (1977)

[15] F. Abe, et al., *Observation of Top Quark Production in $\overline{p}p$ Collisions with the Collider Detector at Fermilab*, Phys. Rev. Lett. **74**, 2626 (1995)

[16] S. Abachi, et al., *Search for High Mass Top Quark Production in $p\overline{p}$ Collisions at $\sqrt{s} = 1.8\ TeV$*, Phys. Rev. Lett. **74**, 2422 (1995)

[17] M. L. Perl, et al., *Evidence for Anomalous Lepton Production in $e^+ - e^-$ Annihilation*, Phys. Rev. Lett. **35**, 1489 (1975)

[18] K. Kodama, et al., *Observation of tau neutrino interactions*, Physics Letters B **504(3)**, 218 (2001)

[19] E. Fermi, *Tentativo di una Teoria Dei Raggi β*, Il Nuovo Cimento **11(1)**, 1 (1934)

[20] Gargamelle Neutrino Collaboration, *Observation of Neutrino Like Interactions Without Muon Or Electron in the Gargamelle Neutrino Experiment*, Phys.Lett. **B46**, 138 (1973)

[21] D. Mohl, G. Petrucci, S. Van Der Meer, *Physics and Technique of Stochastic Cooling*, Phys.Rept. **58**, 73 (1980)

[22] UA1 Collaboration, *Experimental Observation of Isolated Large Transverse Energy Electrons with Associated Missing Energy at s**(1/2) = 540-GeV*, Phys.Lett. **B122**, 103 (1983)

[23] UA2 Collaboration, *Observation of Single Isolated Electrons of High Transverse Momentum in Events with Missing Transverse Energy at the CERN anti-p p Collider*, Phys.Lett. **B122**, 476 (1983)

[24] UA2 Collaboration, *Evidence for $Z_0 \rightarrow e^+\ e^-$ at the CERN anti-p p Collider*, Phys.Lett. **B129**, 130 (1983)

[25] C. Berger, et al., *Jet analysis of the $\Upsilon(9.46)$ decay into charged hadrons*, Phys. Lett. B **82(3–4)**, 449 (1979)

[26] ATLAS Collaboration, *Measurement of the Higgs boson mass from the H→γγ and H→ZZ* *→4ℓ channels in pp collisions at center-of-mass energies of 7 and 8 TeV with the ATLAS detector*, Phys. Rev. D **90**, 052004 (2014)

[27] CMS Collaboration, *Precise determination of the mass of the Higgs boson and studies of the compatibility of its couplings with the standard model*, Technical Report CMS-PAS-HIG-14-009, CERN, Geneva (2014)

[28] M. Thomson, *Modern Particle Physics*, Cambridge University Press (2013)

[29] B. Povh, et al., *Teilchen und Kerne: Eine Einführung in die physikalischen Konzepte*, Springer-Lehrbuch, Springer Berlin Heidelberg (2013)

[30] K. A. Olive, et al. (Particle Data Group), *Review of Particle Physics*, Chin. Phys. **C38**, 090001 (2014)

[31] C. Berger, *Elementarteilchenphysik: Von den Grundlagen zu den modernen Experimenten*, Springer-Lehrbuch, Springer Berlin Heidelberg (2014)

[32] J. Haffner, *The CERN accelerator complex. Complexe des accélérateurs du CERN* (2013), general Photo OPEN-PHO-ACCEL-2013-056

[33] O. S. Brüning, et al., *LHC Design Report* (2004), 10.5170/CERN-2004-003-V-1

[34] http://hilumilhc.web.cern.ch/about/hl-lhc-project, accessed: 2015-03-30

[35] ATLAS collaboration, *ATLAS: Letter of intent for a general purpose p p experiment at the large hadron collider at CERN* (1992), CERN-LHCC-92-04, CERN-LHCC-I-2

[36] ATLAS Collaboration, *ATLAS: technical proposal for a general-purpose pp experiment at the Large Hadron Collider at CERN*, LHC Tech. Proposal, CERN, Geneva (1994), CERN-LHCC-94-43

[37] V. Frigo, *Atlas detector. Detecteur Atlas.* (1997), aC Collection. Legacy of AC. Pictures from 1992 to 2002.

[38] ATLAS collaboration, *ATLAS pixel detector: Technical design report* (1998), CERN-LHCC-98-13

[39] M. Capeans, et al., *ATLAS Insertable B-Layer Technical Design Report*, Technical Report CERN-LHCC-2010-013. ATLAS-TDR-19, CERN, Geneva (2010)

[40] ATLAS collaboration, *Production and Integration of the ATLAS Insertable B-Layer* (in progress)

[41] ATLAS collaboration, *Operation and performance of the ATLAS semiconductor tracker*, JINST **9**, P08009 (2014)

[42] ATLAS TRT, *The ATLAS Transition Radiation Tracker (TRT) proportional drift tube: Design and performance*, JINST **3**, P02013 (2008)

[43] ATLAS collaboration, *ATLAS liquid argon calorimeter: Technical design report* (1996), CERN-LHCC-96-41

[44] ATLAS collaboration, *The ATLAS electromagnetic calorimeter: Construction, commissioning and selected test beam results*, Nucl.Phys.Proc.Suppl. **150**, 98 (2006)

[45] ATLAS collaboration, *ATLAS calorimeter performance Technical Design Report* (1996), CERN-LHCC-96-40

[46] ATLAS collaboration, *The muon spectrometer of the ATLAS experiment*, Nucl.Phys.Proc.Suppl. **125**, 337 (2003)

[47] W. Leo, *Techniques for Nuclear and Particle Physics Experiments: A How-To Approach*, U.S. Government Printing Office (1994)

[48] W. Shockley, *Currents to Conductors Induced by a Moving Point Charge*, J. Appl. Phys. **9(10)**, 635 (1938)

[49] S. Ramo, *Currents Induced by Electron Motion*, Proceedings of the IRE **27(9)**, 584 (1939)

[50] J. Weingarten, *System Test and Noise Performance Studies at The ATLAS Pixel Detector*, Doctoral Thesis, Bonn University (2007), BONN-IR-2007-10

[51] FE-I4 Collaboration, *The FE-I4B Integrated Circuit Guide*, Unpublished Internal Note (2012)

[52] *Probe Systems PA300IS PA300PS - User Manual M10-123299-02* (2006)

[53] *Picosecond Injection Laser (PiLas) - Owner's Manual Rev. 3.0* (2004)

[54] M. A. Green, *Self-consistent optical parameters of intrinsic silicon at 300 K including temperature coefficients*, Solar Energy Materials and Solar Cells **92(11)**, 1305 (2008)

[55] M. Pfaff, *Dynamic Efficiency Measurements for Irradiated ATLAS Pixel Single Chip Modules*, Diploma Thesis, Georg-August-Universität Göttingen (2011), II. Physik-UniGö-Dipl-2011/05

[56] *Sony CCD Black-and-White Video Camera Module - Operating Instructions* (1999)

[57] http://icwiki.physik.uni-bonn.de/twiki/bin/view/Systems/UsbPix, accessed: 2015-03-30

[58] A. Macchiolo, *private communication*

[59] J. Rieger, *Comparison of Thin n- and p-type Bulk Silicon Sensors*, Master's Thesis, Georg-August-Universität Göttingen (2012), II.Physik-UniGö-MSc-2012/08

[60] C. Jacoboni, et al., *A review of some charge transport properties of silicon*, Solid State Electron. **20(2)** (1977)

Bibliography

76

List of Figures

Danksagung

Zunächst möchte ich mich bei all denjenigen bedanken, die mich während der Anfertigung dieser Masterarbeit unterstützt und motiviert haben.

Ich danke Prof. Dr. Arnulf Quadt, der mir, auch ohne jegliche teilchenphysikalische Erfahrung während meines Bachelors, diese Arbeit angeboten hat. Außerdem möchte ich mich dafür bedanken, dass er sich als Betreuer und Erstkorrekteur der Arbeit angeboten hat und in diversen Meetings immer wertvolle Ratschläge parat hatte. Des Weiteren möchte ich PD Dr. Jörn Große Knetter danken, der sich nicht nur als Zweitkorrekteur dieser Arbeit angeboten hat, sondern auch mit seinem ganzen Expertenwissen für alle Fragen zur Verfügung stand.

Mein Dank gilt außerdem Dr. Jens Weingarten, der sich mit seinem weitreichenden Verständniss in alle Fragen reindenken konnte und sich auch nicht davor gescheut hat bei der Suche nach dem einen kaputten Kabel zu helfen. Auch Julia Rieger möchte ich in diesem Rahmen meinen Dank für die Betreuung aussprechen.

Nicht zu vergessen sind natürlich alle anderen Mitglieder des Hardware-Teams - für all die netten und lustigen Gespräche, Tisch-Kicker Partien und Kaffee-Runden möchte ich mich hiermit bedanken.

Erklärung nach §17(9) der Prüfungsordnung für den Bachelor-Studiengang Physik und den Master-Studiengang Physik an der Universität Göttingen:

Hiermit erkläre ich, dass ich diese Abschlussarbeit selbständig verfasst habe, keine anderen als die angegebenen Quellen und Hilfsmittel benutzt habe und alle Stellen, die wörtlich oder sinngemäß aus veröffentlichten Schriften entnommen wurden, als solche kenntlich gemacht habe.

Darüberhinaus erkläre ich, dass diese Abschlussarbeit nicht, auch nicht auszugsweise, im Rahmen einer nichtbestandenen Prüfung an dieser oder einer anderen Hochschule eingereicht wurde.

Göttingen, den 4. April 2017

(Julien-Christopher Beyer)